



HAL
open science

Dome permeability and fluid circulation at La Soufrière de Guadeloupe implied from soil CO₂ degassing, thermal flux and self-potential

Amelie Klein, David Jessop, Franck Donnadieu, Joanny Pierre, Roberto Moretti

► To cite this version:

Amelie Klein, David Jessop, Franck Donnadieu, Joanny Pierre, Roberto Moretti. Dome permeability and fluid circulation at La Soufrière de Guadeloupe implied from soil CO₂ degassing, thermal flux and self-potential. *Bulletin of Volcanology*, 2024, 86 (4), pp.26. 10.1007/s00445-024-01713-z . insu-04510119

HAL Id: insu-04510119

<https://insu.hal.science/insu-04510119v1>

Submitted on 30 Sep 2024

HAL is a multi-disciplinary open access archive for the deposit and dissemination of scientific research documents, whether they are published or not. The documents may come from teaching and research institutions in France or abroad, or from public or private research centers.

L'archive ouverte pluridisciplinaire **HAL**, est destinée au dépôt et à la diffusion de documents scientifiques de niveau recherche, publiés ou non, émanant des établissements d'enseignement et de recherche français ou étrangers, des laboratoires publics ou privés.

001
002
003
004
005
006
007
008
009
010
011
012
013
014
015
016
017
018
019
020
021
022
023
024
025
026
027
028
029
030
031
032
033
034
035
036
037
038
039
040
041
042
043
044
045
046

Dome permeability and fluid circulation at La Soufrière de Guadeloupe implied from soil CO₂ degassing, thermal flux and self-potential

Amelie Klein^{1*}, David E. Jessop^{1,2}, Franck Donnadieu¹,
Joanny Pierre³, Roberto Moretti⁴

^{1*}Université Clermont Auvergne, CNRS, IRD, OPGC, Laboratoire
Magmas et Volcans, Clermont-Ferrand, F-63000, France.

²Institut de Physique du Globe de Paris, Université Paris Cité, CNRS,
Paris, France.

³Observatoire Volcanologique et Sismologique de la Guadeloupe, Institut
de Physique du Globe de Paris, Le Houëlmont, Gourbeyre, 97113, France.

⁴Department of Engineering, University of Campania “Luigi Vanvitelli”,
Via Roma 29, Aversa, 81031, Italy.

*Corresponding author(s). E-mail(s): amelie.klein@uca.fr;

Contributing authors: david.jessop@uca.fr; franck.donnadieu@uca.fr;
joanny@ipgp.fr; roberto.moretti@unicampania.it ;

Orcid IDs

Amelie Klein: 0009-0009-1386-4119

David E. Jessop: 0000-0003-2382-219X

Franck Donnadieu: 0000-0001-8293-1340

Roberto Moretti: 0000-0003-2031-5192

Abstract

Quantifying subsurface fluid flows and related heat and gas fluxes can provide essential clues for interpreting the evolution of volcanic unrest in volcanoes with active hydrothermal systems. To better constrain the distribution of current

047 hydrothermal activity, we mapped diffuse soil CO₂ degassing, ground tempera-
048 ture and self-potential covering the summit of La Soufrière de Guadeloupe during
049 2022-23. We identify areas of fluid recharge and the zones and extent of major
050 ascending hydrothermal flows. This paper provides a first estimate for summit
051 ground CO₂ flux of $4.20 \pm 0.86 \text{ t d}^{-1}$, representing about half the CO₂ emissions
052 from the summit fumaroles. We find an extensive area of ground heating of at least
053 $22\,250 \pm 6900 \text{ m}^2$ in size and calculate a total ground heat flux of $2.93 \pm 0.78 \text{ MW}$,
054 dominated by a convective flux of $2.25 \pm 0.46 \text{ MW}$. The prominent summit frac-
055 tures exert significant control over hydrothermal fluid circulation and delimit a
056 main active zone in the NE sector. The observed shift in subsurface fluid circula-
057 tion towards this sector may be attributed to a changing ground permeability
058 and may also be related to observed fault widening and the gravitational sliding
059 of the dome’s SW flank. Our results indicate that the state of sealing of the dome
060 may be inferred from the mapping of hydrothermal fluid fluxes, which may help
061 evaluate potential hazards associated with fluid pressurisation.

062 **Keywords:** hydrothermal unrest, monitoring, diffuse degassing structures, heat and
063 CO₂ flux, subsurface permeability, fluid circulation

064

065

066

Acknowledgements

067

068

069

070

071

072

073

074

075

076

077

078

079

080

081

082

083

084

Declarations

085

086

087

088

089

090

091

092

The authors have no conflicts of interest to declare that are relevant to the content of this article. AK, DJ, FD and JP conducted fieldwork. AK performed all data analyses and prepared the manuscript. RM and DJ conceptualised the preliminary studies of joint soil and CO₂ heat fluxes. DJ and FD supervised AK and helped prepare the manuscript. RM provided critical feedback on the project and its results. All authors revised the manuscript and agreed to its submission.

1 Introduction

A common definition of a volcanic hydrothermal system is an underground aquifer in a volcanic environment where hot and acid magmatic fluids discharged at depth interact with groundwater. These interactions typically manifest at the surface as fumaroles, thermal springs, hot acid lakes or boiling pools (Hochstein and Browne, 2000; Fischer and Chiodini, 2015). Hydrothermal fluid motion within a volcanic edifice is maintained by a quasi-constant supply of heat and gas from the magma reservoir into water circulating at shallower depths in the brittle, fractured and permeable host rock (Hedenquist and Lowenstern, 1994).

Convection of hydrothermal fluids can create a multitude of non-magmatic unrest signals, e.g. soil and fumarolic degassing, ground heating and deformation, volcano-tectonic seismicity (Rouwet et al, 2014; Pritchard et al, 2019). Additionally, hydrothermal systems modulate geochemical and geophysical signals of magmatic origin, making the interpretation of anomalies in monitoring data and consequently, eruption forecasting difficult (Barberi et al, 1992; Rouwet et al, 2014).

Hydrothermal fluids are enriched in the most water-soluble and acidic components of magmatic gases, e.g. SO_2 , H_2S , HCl and HF (Hochstein and Browne, 2000; Fischer and Chiodini, 2015) promoting intense leaching and alteration (argillisation) of the host-rock. Host rock porosity/permeability is modified by alteration, either increasing or decreasing according to the type of alteration. Porosity-increasing alteration is thought to reduce rock strength and thus edifice stability (López and Williams, 1993; Watters et al, 2000; Farquharson et al, 2019; Heap et al, 2021b), whereas porosity-decreasing alteration (sealing) increases rock strength whilst simultaneously decreasing outgassing, impeding fluid circulation and heat transfer to the surface and enhances pore fluid pressurisation (Heap et al, 2019).

Alteration promotes edifice instability and increases the likelihood of (partial) flank collapses (López and Williams, 1993; Reid et al, 2001; Reid, 2004), potentially causing sudden decompression of the hydrothermal system and laterally-directed blasts (cf. c. 3100 years B.P. event at La Soufrière de Guadeloupe, Boudon et al, 1984; Soufrière Hills, Montserrat, 1997 Sparks et al, 2002). Pore pressurisation can furthermore increase volcano spreading (Heap et al, 2021a) known to promote flank collapses (van Wyk de Vries and Francis, 1997; Karstens et al, 2019) and lead to highly explosive phreatic/phreato-magmatic activity and associated pyroclastic density currents (Heap et al, 2019, 2021a).

Circulating hot fluids with excess electrical charge within the volcanic edifice are evidenced by ground thermal anomalies, increased soil gas emanation, and changes in electric potential at the surface. A widely used method to quantify subsurface fluid flow in volcano-hydrothermal zones and to outline the extent and state of hydrothermal systems is self-potential (SP) mapping (e.g. Massenet and Pham, 1985; Zlotnicki et al, 1994; Finizola et al, 2002; Barde-Cabusson et al, 2012; Brothelande et al, 2014). SP is a passive technique that measures the naturally occurring difference in electrical potential between two electrodes placed at the ground surface. SP signals can have a variety of origins, including electrochemically-generated potentials (redox potentials in ore bodies and contaminant plumes, ion diffusion due to concentration gradients; Jouniaux et al, 2009), potentials produced by thermoelectric effects (Nourbehecht, 1963; Corwin and Hoover, 1979) and electrokinetic (streaming) potentials generated by the

093
094
095
096
097
098
099
100
101
102
103
104
105
106
107
108
109
110
111
112
113
114
115
116
117
118
119
120
121
122
123
124
125
126
127
128
129
130
131
132
133
134
135
136
137
138

139 flow of water through a porous material. Whilst different mechanisms can coex-
140 ist, theoretical considerations by Corwin and Hoover (1979) imply that streaming
141 potentials are larger by about an order of magnitude than thermoelectric and elec-
142 trochemical potentials and there is general agreement that streaming is the main
143 cause of SP anomalies on active volcanoes (Massenet and Pham, 1985; Zlotnicki
144 et al, 1994; Finizola et al, 2002, 2004; Aizawa, 2008; Aizawa et al, 2009; Barde-
145 Cabusson et al, 2012). For a detailed explanation of how streaming potentials are
146 generated, the reader may refer to the papers of Revil et al (1999), Revil (2002),
147 and Jouniaux and Ishido (2012). In general, for typical pH conditions at active
148 volcanoes, the presence of an electrical double layer at the interface between the
149 host rock and the pore water will lead to a net transport of positive ions, and
150 thus the generation of a positive electric potential in the flow direction of the pore
151 water (Revil, 2002). Therefore, on many active volcanoes, positive SP anomalies
152 on the order of a few hundred mV are observed in the summit (crater) area of the
153 edifices or above flank fissures and vents due to the upwelling of hydrothermal
154 fluids, while on the flanks the percolation of meteoric water produces negative
155 anomalies (Finizola et al, 2004; Jouniaux and Ishido, 2012).

156 The convection of fluids from depth transports heat to the surface, particu-
157 larly in a hydrothermal setting. Rising hydrothermal fluids are either emitted by
158 fumaroles where the permeability of the subsurface is high and/or fracture net-
159 works form natural conduits to the surface (Stevenson, 1993) or by diffuse soil
160 degassing in low-permeability zones. Given that H₂O is by far the most abundant
161 chemical species at 90–95 wt.%, and that it has some of the largest values of heat
162 capacity and latent heat of any fluid, transport by water is the dominant mode of
163 heat transfer at hydrothermal systems (Harris, 2013; Fischer and Chiodini, 2015).
164 In low-permeability zones, the condensation of steam at the near subsurface lib-
165 erates significant amounts of heat that is then transported to the surface, leading
166 to ground heating (Aubert, 1999; Harris et al, 2009; Gaudin et al, 2015) and the
167 emission of gas species, mainly CO₂, which do not condense at near-atmospheric
168 conditions given their very low solubility. Thus, if measurements of either i) the
169 surface temperature (e.g. with a thermal camera) or ii) the soil temperature pro-
170 file are performed, the heat flux can be estimated using the thermal properties
171 of the soil. Both techniques have been used in various hydrothermal volcanic set-
172 tings (e.g. Aubert, 1999; Lewis et al, 2015; Gaudin et al, 2016; Jessop et al, 2021).
173 In contrast, soil CO₂ together with the CO₂/H₂O ratio (often derived from anal-
174 yses of fumarole gas samples) can be used to estimate total heat flux in diffuse
175 degassing zones (Chiodini et al, 2001, 2005). Hence, in many volcanic environ-
176 ments, diffuse CO₂ degassing correlates with soil temperature anomalies and SP
177 maxima (Lewicki et al, 2003; Finizola et al, 2010; Byrdina et al, 2014). Combin-
178 ing measurements of CO₂ degassing and soil temperature with SP can provide
179 information on subsurface permeability (controlled by inherent host rock prop-
180 erties, the presence of fault/fracture networks and alteration processes, Grob-
181 be and Barde-Cabusson, 2019) and help to outline the geometry of the hydrother-
182 mal system and constrain fluid circulation (e.g. Matsushima et al, 1990; Finizola
183 et al, 2002; Lewicki et al, 2003; Finizola et al, 2004; Brothelande et al, 2014).

184 As recently demonstrated by the deadly events at Mount Ruapehu (New
Zealand, 2007 Kilgour et al, 2010), Ontake volcano (Japan, 2014, Maeno et al,
2016) and Whakaari (White Island, New Zealand, 2019, Dempsey et al, 2020),
even purely steam-driven/hydrothermal eruptions can be very hazardous given

their sudden onset. Therefore, monitoring the spatial distribution and temporal evolution of hydrothermal signals at volcanoes with long-lived hydrothermal activity is critical to detect and interpret precursory signals of explosive activity.	185
	186
	187
This study focuses on La Soufrière de Guadeloupe (Lesser Antilles), an active andesitic volcano with a well-developed hydrothermal system, that has been showing signs of growing unrest (HCl-rich summit degassing, formation of new summit fumaroles, deformation, fracture opening, seismicity and increased ground heat flux on the summit) (Komorowski et al, 2005; Allard et al, 2014; Villemant et al, 2014; Tamburello et al, 2019; Moretti et al, 2020a; Jessop et al, 2021) since 1992.	188
	189
	190
	191
	192
	193
Here we present for the first time combined mapping of self-potential (SP), subsurface ground temperature and soil diffuse CO ₂ flux on the summit of La Soufrière dome. Interpolated maps of these data show the main zones of rain infiltration into the hydrothermal system and zones of ascending flows. From our data we estimate the heat loss at the summit and, further, the condensation depth of the ascending hydrothermal vapour, which indicates the ground permeability distribution. Our results allow us to infer spatial changes in shallow hydrothermal fluid flow and ground permeability.	194
	195
	196
	197
	198
	199
	200
	201
	202
	203
	204
	205
	206
	207
	208
	209
	210
	211
	212
	213
	214
	215
	216
	217
	218
	219
	220
	221
	222
	223
	224
	225
	226
	227
	228
	229
	230

231
232
233
234
235
236
237
238
239
240
241
242
243
244
245
246
247
248
249
250
251
252
253
254
255
256
257
258
259
260
261
262
263
264
265
266
267
268
269
270
271
272
273
274
275
276

2 Geological setting and background

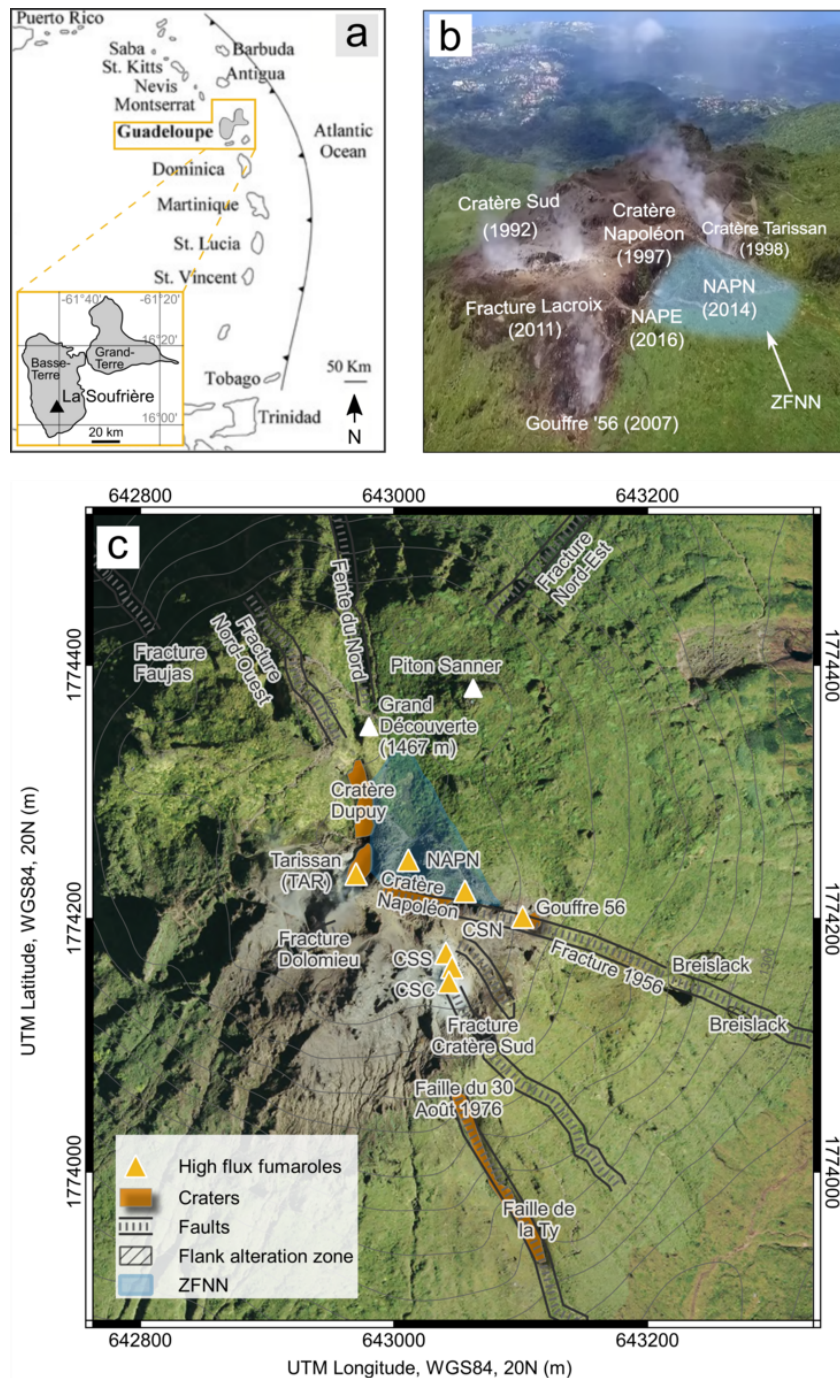


Fig. 1 (a) Schematic map showing the location of Guadeloupe in the Lesser Antilles arc and La Soufrière de Guadeloupe volcano in the southern part of Basse Terre island. Guadeloupe is situated in the central Lesser Antilles arc, where the Atlantic plate subducts under the Caribbean plate. Guadeloupe comprises two main islands: Grand-Terre, associated with the inactive outer arc and Basse-Terre, associated with the active inner arc (Adapted from Allard et al (2014); Pichavant et al (2018)). (b) Aerial photo (A. Anglade, OVSG-IPGP, 2016) of the summit area showing vegetation die-off due to acid degassing. Labelled are the main active fumaroles with the date of reactivation/appearance in brackets. NAPE and NAPN denote the Napoléon Est and Napoléon Nord fumaroles, respectively. The blue shading highlights the zone that has undergone recent changes in ground heating, degassing, and spreading (ZFNN: Zone Fumerollienne Napoléon Nord, since it spreads in the area around NAPN). (c) Map of the summit of La Soufrière de Guadeloupe showing the main geological features mentioned in the text. Main fumaroles indicated by the yellow triangles: Cratère Sud-Sud (CSS), Cratère Sud-Centre (CSC), Cratère Sud-Nord (CSN), Gouffre '56, Napoléon Est (NAPE), Napoléon Nord (NAPN), Tarissan (TAR). ZFNN (Zone Fumerollienne Napoléon Nord) denotes the recent spreading ground heating and diffuse degassing area. Isocontours (grey lines) are plotted every 20 m. The base map is the 2017 IGN aerial orthophoto (IGN, BD ORTHO 2017)

277
278
279
280
281
282
283
284
285
286
287
288
289
290
291
292
293
294
295
296
297
298
299
300
301
302
303
304
305
306
307
308
309
310
311
312
313
314
315
316
317
318
319
320
321
322

323 La Soufrière de Guadeloupe (16.0446° N, 61.6642° W, 1467 m a.s.l., hereafter
324 referred to as La Soufrière) is an andesitic volcano situated in the central part of
325 the Lesser Antilles island arc, where the North American plate subducts under
326 the Caribbean plate (Feuillet et al, 2002). It is the youngest edifice of the Grande
327 Découverte volcanic complex (445 kyr) on the southern Basse-Terre island of
328 Guadeloupe and was emplaced during the last major magmatic eruption in 1530
329 AD (Boudon et al, 2008). Since this last magmatic event, extensive hydrothermal
330 activity has persisted on and around the current lava dome and La Soufrière has
331 experienced six phreatic eruptions, two of which were major events in 1797/98 and
332 1976/77 (Komorowski et al, 2005). Historic phreatic eruptions opened numerous
333 (mostly radial) fractures and vents (Komorowski et al, 2005) on the dome whose
334 evolution and degassing are routinely monitored and sampled by the Observa-
335 toire Volcanologique et Sismologique de Guadeloupe (OVSG-IPGP) along with
336 seismic activity, surface displacements and weather conditions on the summit.

337 After the most recent and largest eruptive crisis in 1976/77, which led to the
338 evacuation of more than 70 000 people and severe socio-economic problems for
339 Basse-Terre (Komorowski et al, 2005; Hincks et al, 2014), the volcano became
340 quiescent with only low-level fumarolic degassing along the Ty fault at the SW
341 base of the dome (Zlotnicki et al, 1994) until 1992 when it entered a new unrest
342 phase. Since 1992, degassing of summit fumaroles has been progressively increas-
343 ing (year of fumarole reactivation indicated in Fig. 1b), concurrently with shallow
344 seismicity, ground deformation, emission of chlorine-enriched acid gases, reactiva-
345 tion of thermal springs at the base of the dome, fumarole and ground temperature
346 and the formation of boiling acid ponds at Cratère Sud (CS) (consisting of 3
347 vents aligned along a fracture: Cratère Sud Sud/Centre/Nord, CSS/CSC/CSN,
348 1997-2003, see Fig. 1) and Cratère Tarissan (TAR, since 2001, Fig. 1 and see
349 also Zlotnicki et al (1992); Komorowski et al (2005); Villemant et al (2014);
350 Rosas-Carbajal et al (2016); Moretti et al (2020a)).

351 Until 2014 soil degassing and ground thermal anomalies on the summit were
352 limited to the areas directly surrounding the major fumaroles (i.e. CS, TAR,
353 Cratère Napoléon, see Fig. 1 and Allard et al, 2014; Gaudin et al, 2016; Tam-
354 burello et al, 2019). However, the area affected by degassing and ground heating
355 has been expanding in recent years and new high-flux fumaroles have appeared:
356 Napoléon Nord, NAPN, in 2014 and Napoléon Est, NAPE, in 2016 (see Fig. 1
357 OVSG-IPGP 2014–2023¹ and Moretti et al, 2020a). Observed changes are partic-
358 ularly strong in an area around NAPN named the Zone Fumerolienne Napoléon
359 Nord (ZFNN) delimited to the west by Cratère Dupuy and TAR (Fig. 1). In that
360 zone, vegetation die-off has been extending concomitant with increased ground
361 heat output (OVSG-IPGP 2014–2023 and Jessop et al, 2021).

362 The first mapping and estimation of La Soufrière heat and mass fluxes was
363 carried out in 2010 (Gaudin et al, 2016). Jessop et al (2021) performed a recent
364 analysis of the total heat flux discharged by the volcano (integrating data span-
365 ning 2000–2019) and compared estimated heat and mass fluxes for 2010 and 2019.
366 The main change observed over this period is the emergence of the ground thermal
367 anomaly at the summit, the ZFNN, which has led to an increase in ground heat
368 flux by an order of magnitude (2010: 0.2 ± 0.1 MW, 2019: 5.7 ± 0.9 MW). Together
369 with the appearance of new fumaroles (NAPN, NAPE) as well as extensive vegeta-
370 tion die-off on the summit, the total volcanic heat output was estimated to

¹<http://www.ipgp.fr/fr/ovsg/bulletins-mensuels-de-lovsg>

have increased from 29.8 ± 8.3 MW in 2010 to 36.5 ± 7.9 MW in 2020 (Jessop et al, 2021).
 A peak in unrest in 2018 (ML 4.1 earthquake) was interpreted as being the result of an increased supply of magma-derived fluids to the hydrothermal system, whose pressure build-up could be released since the dome was sufficiently permeable/fractured (Moretti et al, 2020a). Extensive hydrothermal activity at La Soufrière is sustained by heat and gas fluxes from a 6–7 km deep (i.e. below the summit) andesitic magma reservoir (Feuillard et al, 1983; Hirn and Michel, 1979; Allard et al, 2014; Pichavant et al, 2018; Metcalfe et al, 2022) to the deep aquifer (i.e. ≈ 1 km b.s.l. or 2.5 km below the summit) (Moretti et al, 2020a, and references therein). Deep, boiling hydrothermal fluids and magma-derived gases then rise through fractures, interact with groundwater at shallower depths (average rainfall summit: $5\text{--}6$ m yr⁻¹, (OVSG-IPGP, 2012–2023) and feed summit fumaroles (Villemant et al, 2014; Moretti et al, 2020a; Moune et al, 2022). Shallow hydrothermal activity (i.e. ≤ 1.5 km below the summit) is considered responsible for the observed shallow deformation and seismicity (Moretti et al, 2020a) and increasing fluxes of rising acid fluids have caused extensive alteration (progressive sealing) and mechanical weakening of the dome (Komorowski et al, 2005; Salaün et al, 2011; Rosas-Carbajal et al, 2016; Heap et al, 2021b). These observations cause concern regarding the collapse of the SW flank, already showing surface displacements of up to 9 mm yr⁻¹ towards the SW (Moretti et al, 2020a, OVSG-IPGP 1996–2023), which would not only directly affect the increasingly populated southern slopes, where more than 50 000 people reside, but could also decompress the hydrothermal system leading to explosive phreatic activity (Komorowski et al, 2005; Moretti et al, 2020a).

3 Methods

To better constrain the distribution of presently active hydrothermal zones on the dome, we have, for the first time, conducted self-potential, temperature and diffuse CO₂ flux surveys over a relatively short ≈ 1 year duration. SP and temperature measurements were carried out at the summit area of La Soufrière (Fig. 1) during a field campaign in May/June 2022 under overall constant, humid weather conditions but without any major rainfall. Due to instrument issues in 2022, soil CO₂ flux (ϕ CO₂) data were acquired during another campaign in May 2023 under mostly dry weather conditions. All the data were located using a handheld GPS receiver (Garmin eTrex[®] 20 and Garmin GPSMAP[®] 60) as well as internal GPS in the CO₂ flux meter. To facilitate data analysis, all data sets were interpolated using the sequential Gaussian simulation (sGs) algorithm within the open-source Stanford Geostatistical Modeling Software (SGeMS) (Remy et al, 2009) and following the methods of Cardellini et al (2003). 250 simulations were performed for each data set using simulation grids with 5 m node spacing. The variograms of the normal score transformed data and fitted variogram models can be found in Fig. 10. The produced realisations were post-processed to obtain E-type (E: expected value) maps. The E-type map, i.e. the map of the mean at all grid nodes, is obtained through pointwise linear averaging of all the realisations. The maps of E-type (mean) are reported in Fig. 2, 4, 6, 9; they were used to calculate the reported heat and CO₂ fluxes and to define the extent of the heated and diffuse degassing area.

415 **3.1 Temperature profiles, gradient and heated area**
416 **calculations**

417 Temperature data were acquired at a mean spacing of 11 m (maximum of 48 m),
418 with a generally higher density of data points east of Cratère Dupuy and
419 TAR. Ground temperatures were measured along vertical profiles at the sur-
420 face, at 20 and 60 cm depth using three PT100 platinum resistance thermometers
421 (measurement accuracy $\pm 1^\circ\text{C}$) embedded in a thermal paste in stainless-steel,
422 ground-penetrating spikes. The thermal probes, built at the OVSG-IPGP, were
423 connected to a portable data logger that took readings in real-time at 1 Hz.
424 Before each temperature measurement, we hammered a steel bar (approx. 2 cm
425 diameter) into the ground to the respective depths. We then inserted the ther-
426 mal probes into the holes created and took readings when the temperature had
427 stabilised. Error on the depth of probe insertion was less than 5 cm.

428 We obtained estimations of temperature variation with depth x using a linear
429 model

$$430 T(x) = ax + b, \tag{1}$$

431 where $dT/dx = a$ is the prediction of the temperature gradient and $T(0) = b$ is
432 the predicted surface temperature. For each measurement site, we estimated the
433 coefficients a and b using a weighted linear least-squares method, with weights
434 derived from the uncertainty of depth measurements (typically ± 0.5 cm).

435 We calculated the heated area from the interpolated map shown in Fig. 4 using
436 the threshold of the background temperature, $T_{\text{background}} = 22^\circ\text{C}$ (cf. Fig. 3).
437 This procedure yielded a binary image where the non-zero pixels represented the
438 heated area. The heated area is thus the number of non-zero pixels multiplied by
439 the resolution of the sGs map, 25 m^2 . To obtain an error bound on the calculated
440 heated area, we considered that the natural isotherm is discretised by the perime-
441 ter of the heated area and will cut through the pixels of the boundary. Thus
442 we calculated the discrete heated area perimeter using a Laplace edge-detection
443 algorithm with a 3-pixel kernel. The number of perimeter pixels again multiplied
444 by the image resolution plus the standard deviation of the ground temperature
445 from the 250 realisations gives our error bound.

446 **3.2 CO₂ measurements**

447 We performed soil diffuse CO₂ degassing measurements following the accumu-
448 lation chamber method as described in detail by Chiodini et al (1998). This is
449 an established method for measuring soil CO₂ flux in volcanic areas, whose reli-
450 ability has been tested both under laboratory conditions and in the field (e.g.
451 Chiodini et al, 1996, 1998; Cardellini et al, 2017). Specifically, we used a West
452 Systems[®] flux meter attached to a type B accumulation chamber consisting of
453 a cylindrical chamber (20 cm inlet diameter, 19.8 cm internal chamber height),
454 an IR spectrometer (LI-COR CO₂ detector LI-830 with accuracy within 3% of
455 reading, and measurement range 0–20 000 ppm CO₂), and an AD converter. A
456 Bluetooth-connected smartphone managed the flux meter. Chiodini et al (1998)
457 report a reproducibility error of the accumulation chamber method of less than
458 $\pm 10\%$, consistent with the manufacturer’s (West Systems) stated measurement
459 accuracy of $\pm 10\%$ in high flux zones ($> 60\text{ g m}^{-2}\text{ d}^{-1}$) and $\pm 25\%$ in low flux
460 zones ($< 60\text{ g m}^{-2}\text{ d}^{-1}$). Our measurements were taken at a mean spacing of 15 m

(minimum of 3 m, maximum of 35 m). We were not able to perform measurements on a regular grid (cf. Cardellini et al, 2003) owing to the rugosity of the terrain, though we achieved a higher density of measurements within the ZFNN. The soil CO₂ flux is proportional to the concentration increase in the accumulation chamber over time (120–200 s per measurement). Flux values were derived from the slope of a linear fit of concentration as a function of time.

The diffuse CO₂ degassing area was calculated from the interpolated map shown in Fig. 6 using the median of our CO₂ data ($17.6 \text{ g m}^{-2} \text{ d}^{-1}$) as the threshold for relevant CO₂ degassing. The CO₂ degassing area is thus the number of pixels with a CO₂ flux above $17.6 \text{ g m}^{-2} \text{ d}^{-1}$ multiplied by the resolution of the sGs map, 25 m^2 . The error bound of the degassing area was obtained following the same process as for the heated area. The estimated total uncertainty of the reported area accounts for the uncertainty of the perimeter of degassing pixels, uncertainty in the CO₂ measurement and the standard deviation of CO₂ flux from the 250 realisations.

3.3 Self-potential

SP values were taken at a mean spacing of 6 m (typical range 5–15 m, maximum spacing 29 m) over the summit area. The measuring equipment consisted of a digital voltmeter (10 GΩ input impedance, 1 mV sensitivity), two non-polarising Cu/CuSO₄ electrodes and a 500 m long insulated cable. Before starting the measurements, the electrodes were placed tip to tip to check for a voltage $\Delta U \leq 1 \text{ mV}$ and several SP measurements were performed in a small area around the reference location to ensure the correctness of the SP values. The electrodes were placed at a depth of 5–10 cm, which usually was enough to get good contact with the ground. All SP data were closure corrected following Barde-Cabusson et al (2021), distributing the drift (a few mV over the duration of 2–5 hours) linearly over the loops. Elevation changes are known to induce variations in SP readings due to vertical distance between the surface and the water table ('topographic effect'), typically leading to a negative linear relationship between SP and elevation in the hydrogeological zones (flanks) of active volcanoes (Lénat, 2007). Since we only measured on the summit and given the small elevation changes of < 40 m over our study area, this effect was minimal and we did not correct our data for topography-induced variations.

4 Results

4.1 Self-potential map of the summit

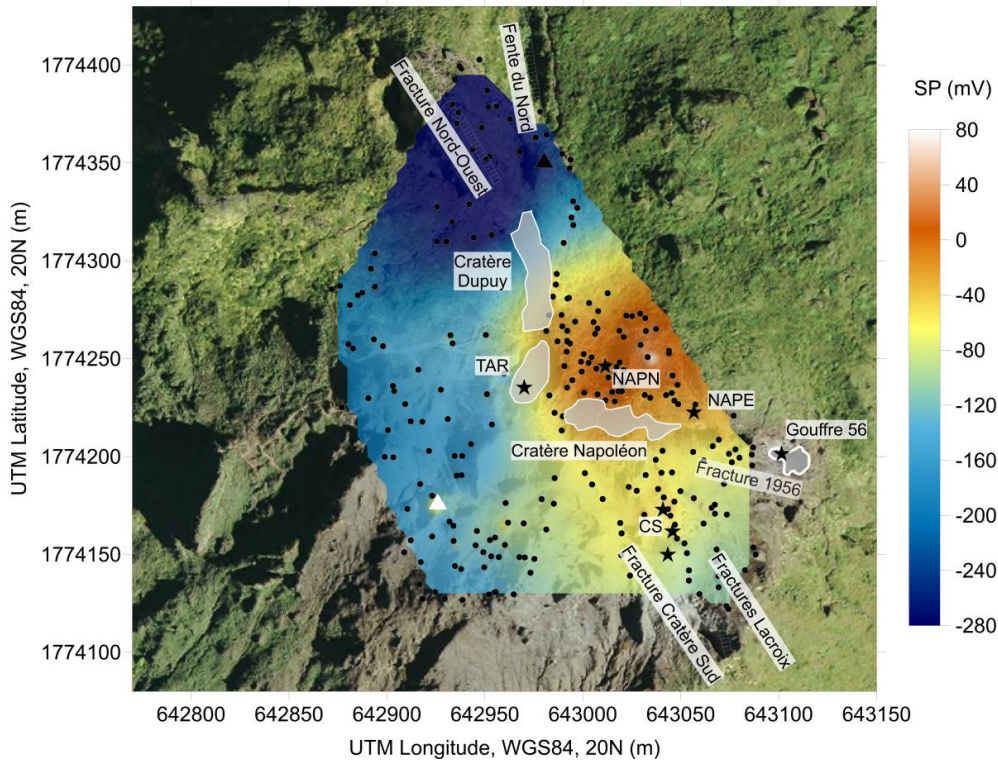


Fig. 2 Interpolated (sGs) map of self-potential (SP) superimposed on an orthophoto of the summit area of La Soufrière de Guadeloupe (background image is IGN, BD ORTHO 2017). The map shows the average SP of the 250 realisations in individual model cells (5×5 m). Black dots display the SP measurement points, the white triangle shows the location of the reference electrode. Stars indicate the main summit fumaroles: Cratère Sud (CS), Gouffre '56, Napoléon Nord (NAPN), Napoléon Est (NAPE) and Tarissan (TAR). The area east of Cratère Dupuy/TAR and north of Cratère Napoléon is denoted ZFNN (cf. Fig. 1b and c)

We performed SP measurements covering the entire summit area of La Soufrière to constrain zones of hydrothermal upwelling and rain infiltration, respectively. The resulting SP map (Fig. 2) shows an overall negative signal except for a localised area delimited by Fracture Napoléon to the south and Cratère Dupuy/-Tarissan to the west (ZFNN). This overall negative signal is expected on such a highly fractured and humid volcano, where meteoric infiltration is large (average annual rainfall 2016–2021: 4.5 m. OVSIG-IPGP, 2016–2021; Vaerewyck, 2022).

The highest negative anomaly is located north of Cratère Dupuy where rocks at the surface are mostly unaltered and the vegetation is intact suggesting no

recent or past hydrothermal activity at the surface. Contrastingly, the southern areas of the summit contain surface rocks that are strongly argillised, implying lower ground permeability that could explain less negative SP than in the northern zone due to less effective rain infiltration. Moreover, we observe more negative values (range: -352 to -44 mV) west of Cratère Dupuy/TAR as opposed to the eastern part of the summit area, where values range between -270 and 84 mV. This is in agreement with the absence of fumaroles/ diffuse degassing west of Cratère Dupuy, whereas there are several sites of strong degassing in the eastern part of the summit (CS, NAPN, TAR, Gouffre '56), as well as diffuse degassing (ZFNN). Positive SP values are all located in the ZFNN. They suggest local ascent of hydrothermal fluids and relatively high ground permeability/fracturing. The positive anomaly extends to the edge of the vegetation in the east of the survey area. Given visible degassing and locally heated ground within the vegetation east of the surveyed area, it most probably also spreads into the vegetation, which is consistent with the observed progressing vegetation die off (OVSG-IPGP, 2014–2022).

4.2 Ground heating and temperature gradients at the summit

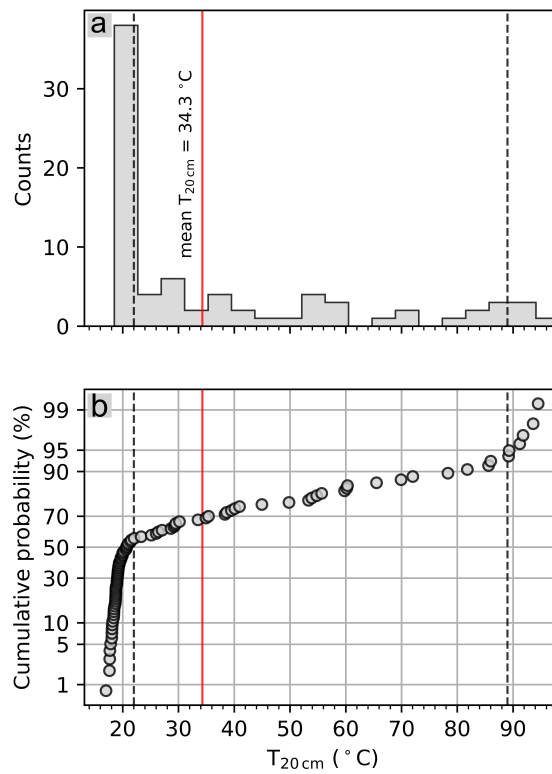
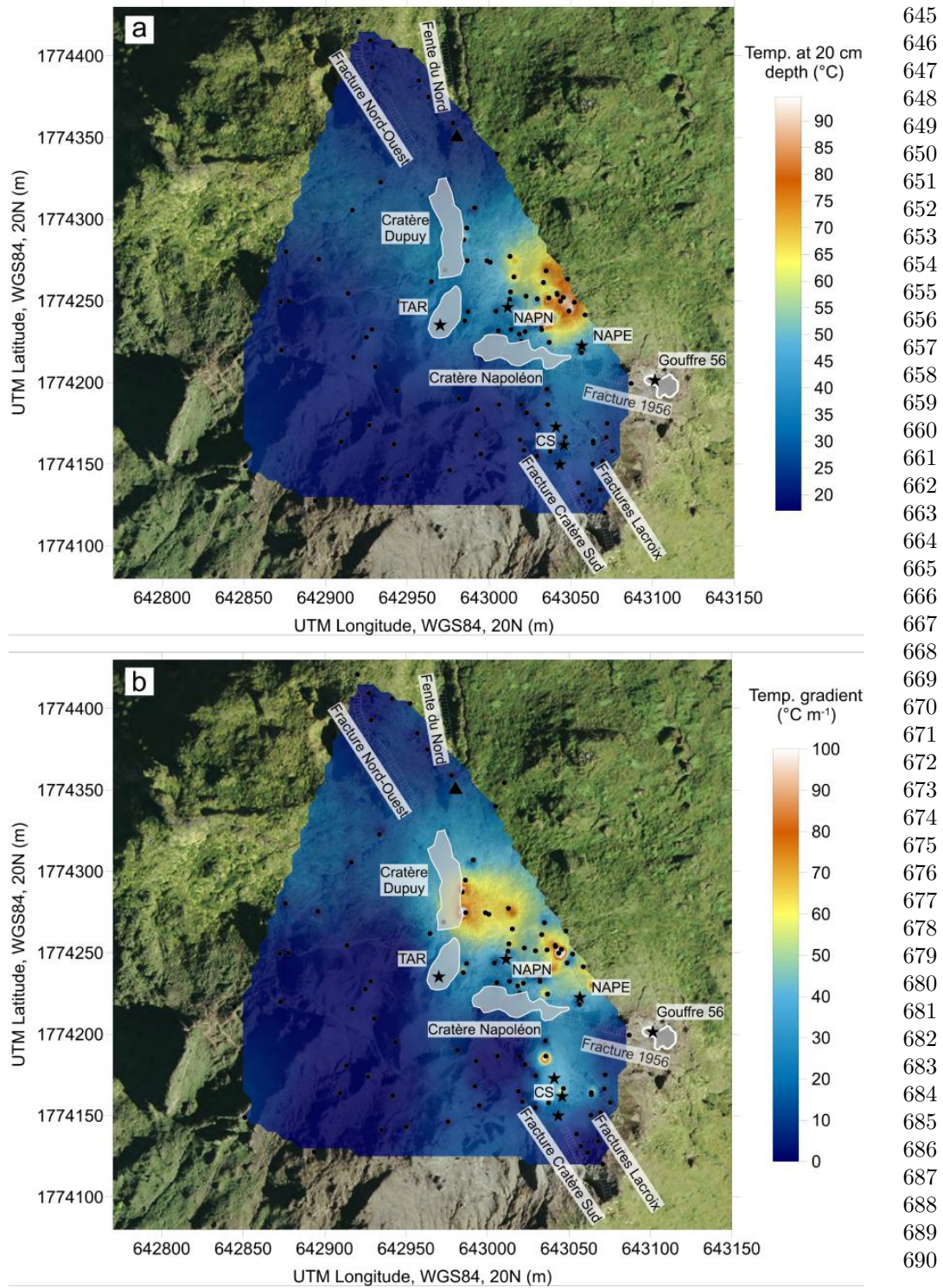


Fig. 3 (a) Histogram and (b) probability plot of the temperature data at 20 cm depth, as presented in Fig. 4a. From the distribution of these data, we identify three populations with cutoff temperatures of 89 and 22 °C, indicated by dashed black lines. The mean temperature at 20 cm depth is indicated by the red line



15
Fig. 4 Interpolated (sGs) maps of (a) ground temperature at 20 cm depth and (b) the ground temperature gradient calculated from (Eq. 1) and temperature measurements at 0, 20 and 60 cm depth. Shown are the mean values of the 250 realisations in individual model cells (5×5 m) superimposed on an orthophoto of the summit area of La Soufrière. Black dots display the locations of temperature measurements; stars indicate the main summit fumaroles: Cratère Sud (CS), Gouffre '56, Napoléon Nord (NAPN), Napoléon Est (NAPE) and Tarissan (TAR). The area east of Cratère Dupuy/TAR and north of Cratère Napoléon is denoted ZFNN (cf. Fig. 1b and c)

691 Measured ground temperatures (Fig. 4a) are highest in the ZFNN, reaching
692 94.5 °C at 20 cm depth. Away from craters and fractures, the ground tempera-
693 ture is close to ambient temperature (only minor effects of solar heating at 20 cm
694 depth expected) varying between approx. 17 and 19 °C. The only exceptions are
695 close to TAR/southern part of Cratère Dupuy (26.4–33.5 °C), around CS (ambi-
696 ent temperature to locally 35.4 °C) and in the ZFNN (20–94.5 °C). The highest
697 temperatures are just below the boiling point of water at this altitude (95.2 °C),
698 suggesting condensation of boiling hydrothermal fluids close to the surface.

699 We show the temperature gradient calculated from Eq. (1) in Fig. 4b. Spa-
700 tially, we observe a similar distribution as per ground temperature. Away from
701 fractures and the hydrothermally active areas, temperature gradients are essen-
702 tially zero. There appears to be some structural control to the temperature
703 gradients and we observe higher values ($> 50 \text{ °C m}^{-1}$) aligning with the major
704 faults (CS/Fente du Nord and Fracture 1956). The highest gradients, i.e. beyond
705 90 °C m^{-1} are found next to Cratère Dupuy, around CS and in the ZFNN with
706 a maximum value of $161.50 \pm 55.12 \text{ °C m}^{-1}$ situated on the border between the
707 ZFNN and Cratère Dupuy.

708 4.3 Soil CO₂ flux at the summit

709 In diffuse degassing areas, soil CO₂ flux often originates from biogenic or volcanic
710 sources, resulting in a bimodal distribution of CO₂ flux values. In a logarithmic
711 probability plot, this is represented as a curve with an inflection point from
712 which background and volcanic populations can be partitioned following Sin-
713 clair’s method (Sinclair, 1974; Chiodini et al, 1998). The absence of obvious
714 inflexion points in the logarithmic probability plot (cf. Fig. 5b) implies a single
715 lognormally-distributed population (Sinclair, 1974; Chiodini et al, 1998; Elío
716 et al, 2016). This indicates that the measured CO₂ flux has a unique volcanic-
717 hydrothermal source and that our data do not include any significant biogenic
718 contribution.

719
720
721
722
723
724
725
726
727
728
729
730
731
732
733
734
735
736

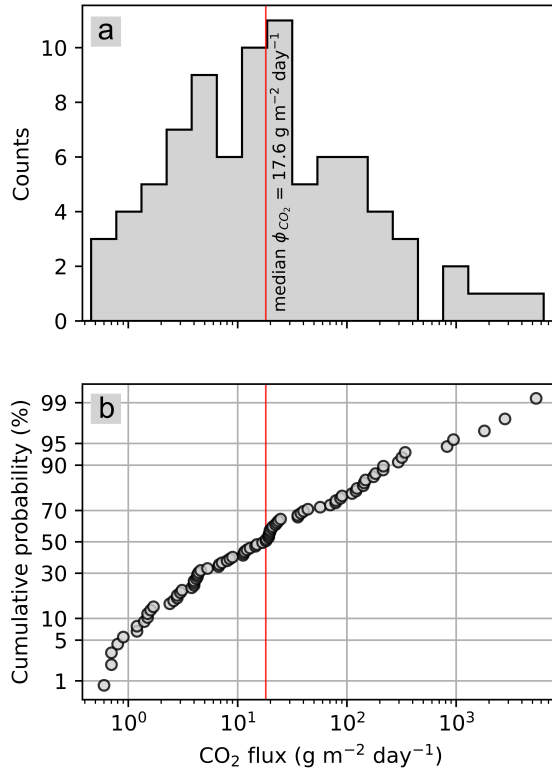
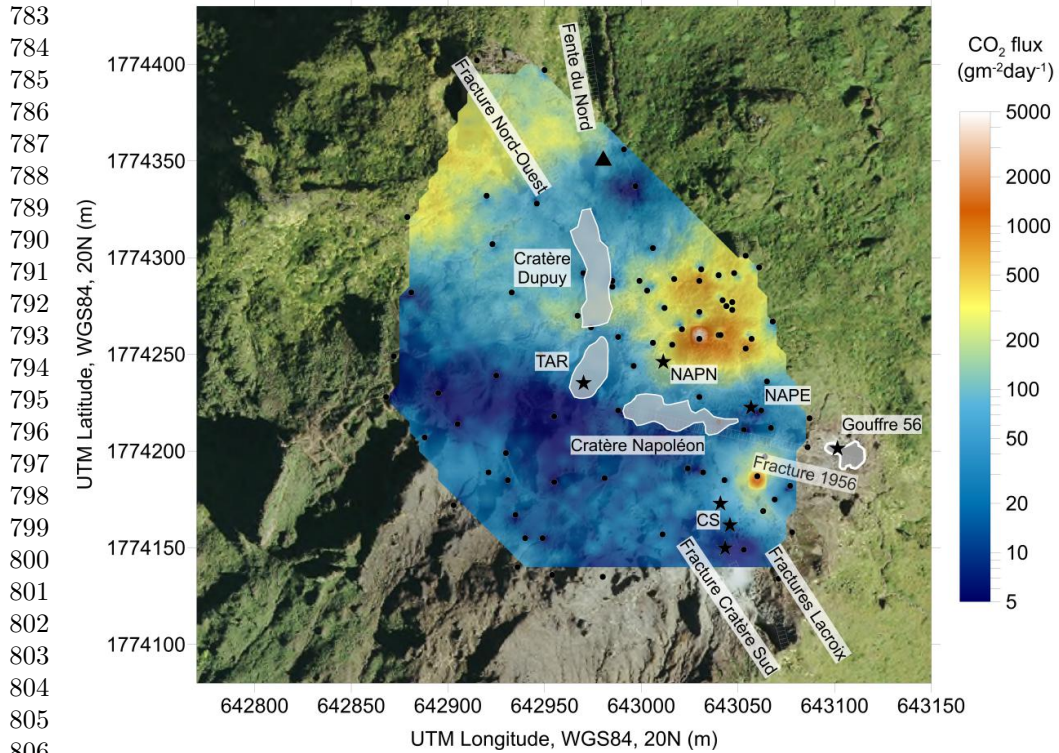


Fig. 5 (a) Histogram and (b) Log probability plot of the soil CO₂ flux data on the summit of La Soufrière. The absence of obvious inflexion points and linear alignment of data points implies a single lognormally-distributed (i.e. unimodal) population (Sinclair, 1974; Chiodini et al, 1998; Elío et al, 2016), indicating that measured CO₂ flux has a unique volcanic-hydrothermal source and that our data do not include any significant background CO₂ flux

737
 738
 739
 740
 741
 742
 743
 744
 745
 746
 747
 748
 749
 750
 751
 752
 753
 754
 755
 756
 757
 758
 759
 760
 761
 762
 763
 764
 765
 766
 767
 768
 769
 770
 771
 772
 773
 774
 775
 776
 777
 778
 779
 780
 781
 782



783
 784
 785
 786
 787
 788
 789
 790
 791
 792
 793
 794
 795
 796
 797
 798
 799
 800
 801
 802
 803
 804
 805
 806
 807
Fig. 6 Interpolated (sGs) map of soil CO₂ flux measurements in May 2023. The map shows the
 808 mean values of the 250 realisations in individual model cells (5 × 5 m) superimposed on an orthophoto
 809 of La Soufrière. Black dots indicate the locations of CO₂ flux measurements; stars indicate the main
 810 summit fumaroles: Cratère Sud (CS), Gouffre '56, Napoléon Nord (NAPN), Napoléon Est (NAPE)
 811 and Tarissan (TAR). The area east of Cratère Dupuy/TAR and north of Cratère Napoleon is denoted
 812 ZFNN (cf. Fig. 1b and c)
 813

814
 815 The distribution of soil CO₂ flux on the summit area of La Soufrière
 816 (Fig. 6) shows variations spanning four orders of magnitude ($0.6 \leq \phi_{\text{CO}_2} \leq$
 817 $5390 \text{ g m}^{-2} \text{ d}^{-1}$). Like SP and temperature (gradient), CO₂ flux is highest in the
 818 ZFNN and in the vicinity of CS ($\phi_{\text{CO}_2} > 200 \text{ g m}^{-2} \text{ d}^{-1}$). CO₂ flux is also punctually
 819 increased ($\phi_{\text{CO}_2} > 100 \text{ g m}^{-2} \text{ d}^{-1}$) close to the large faults Fente du Nord and
 820 Fracture Nord-Ouest, although interpolation is based on very few points in the
 821 north of the survey area. CO₂ fluxes are low ($\phi_{\text{CO}_2} \leq 20 \text{ g m}^{-2} \text{ d}^{-1}$) everywhere
 822 else. As for SP and temperature, we find relatively sharp boundaries between
 823 areas of high and low ϕ_{CO_2} , implying that the ascent of hydrothermal fluids is
 824 controlled by the main fractures. More specifically, Cratère Dupuy/TAR (on the
 825 Fente du Nord - Faille de la Ty line) and Cratère Napoleon on the 1956 Fracture
 826 which delimit the ZFNN anomaly, and Fracture Cratère Sud and the Fractures
 827 Lacroix that control fluid ascent around CS.

828 Besides this structural control of fluid ascent along major summit faults and
 fractures, we note that also lithological interfaces and topography factors can
 exert control on the ascent pathways of fluids at volcanoes as described for La

Fossa cone, Vulcano (Schöpa et al, 2011). For example, preferential fluid migration might occur at the interface between rock units of different alteration states (and permeabilities) within La Soufrière dome (Rosas2016). However, the resolution of ERT data at La Soufrière (Rosas-Carbajal et al, 2016) is too low to infer any concrete ascent pathway based on alteration states within our survey area. Numerical modelling by Schöpa et al (2011) suggested that the gravitational stress field directs hydrothermal fluids to topographic highs, leading to the preferential occurrence of fumaroles at crater rims, a factor that might be at play in our survey area. The SP, temperature and CO₂ anomalies we observe may thus be associated with a combination of these factors.

5 Discussion

5.1 Spatial shift in hydrothermal fluxes evidenced by SP, ground temperature and soil CO₂

Comparison with previous SP studies at La Soufrière (Pham et al, 1990; Zlotnicki et al, 1994; Brothelande et al, 2014) suggests relative stability of the negative anomalies and thus the main infiltration zones over time. Nevertheless, there is an evolution of the positive anomalies on the summit. Pham et al (1990) found a negative anomaly covering the entire dome with the highest negative anomaly associated with the Faujas and NW fractures, in the northern part of the summit. This finding is consistent with the results of Zlotnicki et al (1994); Brothelande et al (2014) and this work. Concurrent with the reactivation of summit fumaroles beginning in 1992, Zlotnicki et al (1994) observed a positive anomaly from data acquired in 1993 in the southern sector of the summit, between Dolomieu Fracture and the 1956 Fracture, with a maximum just north of CS. This pattern was confirmed in 2011 by Brothelande et al (2014), who found a strong positive SP signal in the SE sector of the summit, a maximum near CS, and positive values stretching to the north until Cratère Dupuy (just south of Faujas and NW fracture; cf. Fig. 4B in Brothelande et al (2014)).

Qualitatively, we see a clear spatial shift in hydrothermal activity. While the area around CS and the entire SE summit sector still show higher values than the western part, we find a maximum anomaly in the ZFNN (just NE of Cratère Napoléon and stretching eastwards into the vegetation). Before 2014, ascending flows indicated by the SP maxima were only constrained to CS and its surroundings, as opposed to major activity in the ZFNN now.

We further note that even though positive and negative SP anomalies are generally interpreted as indicators for upward and downward fluid flow, respectively, this interpretation is not necessarily valid. The polarity of the SP anomalies essentially depends on the so-called zeta potential which describes the electric potential at the mineral-fluid interface in the porous rock and is a key parameter for electrokinetic coupling. The zeta potential is usually assumed to be negative in most Earth Science applications. In our case, the surface charge is compensated by a net positive, mobile charge in the pore fluid, which leads to the positive SP signal in the fluid flow direction. However, certain clay minerals and very acidic pore fluids (Revil, 2002; Hase et al, 2003; Aizawa, 2008; Jouniaux et al, 2009) can

875 result in positive or near zero zeta potentials. As a result, the sign of SP anomalies
876 above ascending hydrothermal fluids may be reversed, or no significant SP
877 anomaly may be observed.

878 As positive and negative potentials are always with respect to the reference
879 point, a quantitative comparison between the various studies is not possible due
880 to the reference electrode being in a different location in each one. Even though we
881 placed our reference in an area with no hydrothermal activity, we do not consider
882 it reasonable to recalculate our mapping to the reference at the base of the dome
883 used by Brothelande et al (2014), given that more than a decade has elapsed
884 between the two campaigns, during which the system has changed considerably.
885 Given that our reference is located on the summit (c.f. Fig. 2) as opposed to the
886 previous campaigns, the boundaries between positive and negative might not be
comparable.

887 Since the pH of hydrothermal fluids sampled at the hot springs surrounding
888 La Soufrière dome and on the summit (monthly sampling by OVSG-IPGP, 2020-
889 2023) is mainly comprised between 2 and 6.5, we assume that the zeta potential is
890 negative, and the sign of SP anomalies is not reversed. That the observed positive
891 SP anomalies coincide with high CO₂ and heat fluxes supports this assumption.
892 Gases at some of the summit fumaroles and the acid point in TAR are however
893 characterised by very acidic fluids (< 1) (OVSG-IPGP, 1992–2023; Inostroza
894 et al, 2022). Therefore, in some zones on the summit and around the dome,
895 ascending hydrothermal fluids may not be associated with a distinct positive SP
896 signal as observed at Faille de la Ty at the southern dome base (Brothelande
897 et al, 2014). SP should therefore be interpreted with caution and in combination
with complementary methods.

898 From the interpolated temperature data (Fig. 4) and taking the cutoff temper-
899 ature of 22 °C (cf. Fig. 3), we find a heated area of $22\,250 \pm 6900\text{ m}^2$ on the
900 summit compared to $14\,070\text{ m}^2$ determined from 2019 aerial thermal imagery
901 (Jessop et al, 2021). This suggests that the heated area outside the vegetated
902 zone has expanded since 2019. In making this comparison, we are aware of the
903 limitations of the two different techniques: aerial thermal images may capture
904 additional hot spots in areas that cannot be reached on foot, and vegetation may
905 obscure the thermal signal which is not a factor for the direct measurements as
906 reported here. We also find that the heated area depends essentially on the choice
907 of background temperature and interpolation method, so by defining 21 °C and
908 23 °C as ambient temperature instead of the chosen 22 °C, we get a heated area of
909 $25\,750 \pm 7200\text{ m}^2$ and $19\,425 \pm 6200\text{ m}^2$, respectively. Kriging yielded an area esti-
910 mate ($12\,400 \pm 3900\text{ m}^2$) much closer to the value reported by Jessop et al (2021).
911 We further note that our temperature survey does not cover the ZFNN tempera-
912 ture anomaly entirely as we were unable to venture into densely-vegetated areas.
913 Based on Fig. 4a) it is likely that the heated area in 2022 extended further to the
914 E and NE into the vegetation and thus our estimate is a minimum value. This
915 is supported by the fact that the SP anomaly reflecting the ascent of hydrother-
916 mal fluids in the ZFNN is likewise cut off at the eastern edge of the surveyed
917 area (vegetation limit, Fig. 2) and by "hot mud" observed at several spots in the
918 vegetation a few tens of meters east of the survey area.

919 Allard et al (2014) performed soil CO₂ degassing measurements using a
920 portable Dräger IR spectrometer coupled to a West System accumulation cham-
ber at the base of the dome and along a N–S profile on the summit in March

2006. They did not detect any ϕCO_2 anomalies on the summit that went beyond the biogenic background flux ($60\text{--}160\text{ g m}^{-2}\text{ d}^{-1}$ in their study) except for a few spots around CS. However, we note that their study was conducted before the formation of the NAPN/NAPE fumaroles and the ZFNN.

In contrast to Allard et al (2014), we detected volcanic CO_2 -flux not only in the vicinity of CS but also along TAR as well as in the ZFNN (Fig. 5b, Fig. 6), which is consistent with the formation of the fumarolic field on the dome summit since at least 2014. Using the median of our CO_2 data ($17.6\text{ g m}^{-2}\text{ d}^{-1}$) as the threshold for relevant CO_2 degassing, we obtain a CO_2 degassing area of $26\,220 \pm 12\,550\text{ m}^2$. This value is consistent with the heated area estimate ($22\,250 \pm 6\,900\text{ m}^2$) and indicates the hydrothermally active area on the summit.

Overall, the high ground temperatures combined with maximum diffuse CO_2 flux and maximum SP values suggest strong hydrothermal fluid circulation below the ZFNN. The maximum SP, ground temperature, and CO_2 values are all located near $643\,035\text{ m E}$, $1\,774\,255\text{ m N}$ (UTM 20N - WGS84), about $25\text{--}40\text{ m}$ to the north-east of NAPN. We note that maximum values (T, soil CO_2 and SP) are delimited by prominent summit fractures: Fente du Nord, Dupuy and TAR to the west and Fracture 1956 /Cratère Napoléon to the south. Future efforts should be directed towards delimiting the eastern edge of subsurface fluid circulation. We interpret the concentration of activity in the NE sector of the summit as a result of increasing ground permeability, allowing hydrothermal fluids to rise through new fracture/pore networks. Increased ground fluxes/permeability in the NE sector may result from a combination of sealing processes affecting the location of increased heat and gas fluxes (proposed by e.g. Harris and Maciejewski (2000), Fossa fumarole field, Vulcano) and the observed opening of Cratère Napoléon (about 5 mm yr^{-1} until 2023) (Moretti et al, 2020a, OVSG-IPGP 2018–2023) as well as radial surface displacements of $2.4\text{--}16.5\text{ mm yr}^{-1}$ (OVSG-IPGP, 2023) on the summit. Extensometry data showed an accelerated opening of W–E fractures cutting the summit (Fracture Napoléon, Faille du 8 Juillet 1976, Breislack) between the end of 2015 and 2021, which is concurrent with the apparition of a new high-flux fumarole (NAPE, 2016) and several low-flux fumaroles scattered over the sector north of Fracture 1956 and east of Cratère Dupuy/TAR (OVSG-IPGP, 1992–2023). These observations could also be related to the sliding of the SW flank as indicated by GNSS velocities in Fig.7 in Moretti et al (2020a) associated with the alteration-induced detachment plane identified by Rosas-Carbajal et al (2016). Overall, these observations suggest a strong control of hydrothermal fluid circulation by the major summit faults /craters, which has also been shown to play an important role at La Fossa cone, Vulcano (Barde-Cabusson et al, 2009) and Aluto volcano, Main Ethiopian Rift (Hutchison et al, 2015). However, variations in lithology/alteration and the topography may influence surface permeability and the final distribution of hydrothermal anomalies at the surface (compare Schöpa et al (2011), La Fossa, Vulcano; Hutchison et al (2015), Aluto volcano, Main Ethiopian Rift).

5.2 Total soil CO_2 and heat fluxes

Integrating our ϕCO_2 data over the exhaling area, we find a total soil CO_2 flux of $4.20 \pm 0.86\text{ t d}^{-1}$. Moune et al (2022) found an average CO_2 flux for CS+Gouffre '56+TAR fumaroles in the 2018–2020 period of 0.094 kg s^{-1} (8.13 t d^{-1}), meaning that diffuse degassing is equivalent to about half the CO_2 emissions from summit

967 fumaroles. Thus, diffuse degassing represents an important contribution to the
968 CO₂ budget for La Soufrière de Guadeloupe.

969 We attempt to estimate the heat flux as

970
971
$$Q = \int_A (Q_{\text{cond}} + Q_{\text{conv}}) dA, \quad (2)$$

972
973

974 where A is the survey area. The conductive heat flux, Q_{cond} is given by Fourier's
975 law

976
$$Q_{\text{cond}} = k \frac{dT}{dx}, \quad (3)$$

977 where k is the thermal conductivity. Heap et al (2022) determined thermal con-
978 ductivities for La Soufrière andesite according to their state of alteration and
979 found $0.6 \text{ W m}^{-1} \text{ K}^{-1} \leq k \leq 1.6 \text{ W m}^{-1} \text{ K}^{-1}$ for highly-altered and low alter-
980 ation rock. Thermal conductivity for partially-saturated unlithified samples from
981 La Soufrière was found to be around $1 \text{ W m}^{-1} \text{ K}^{-1}$ (Heap et al, 2023), and
982 such material was encountered at the majority of measurement sites. We use
983 $k = 0.6 \text{ W m}^{-1} \text{ K}^{-1}$ and $k = 1.6 \text{ W m}^{-1} \text{ K}^{-1}$ in eq. (3) to calculate a typical value
984 for Q_{cond} using the data shown in Fig. 4b) and find $Q_{\text{cond}} = 0.69 \pm 0.30 \text{ MW}$,
985 using the area covered by our ground temperature measurements.

986 However, as illustrated in Fig. 7, using a linear model to fit temperature
987 gradients will systematically underestimate the surface gradient and thus the
988 derived heat flux in areas with high hydrothermal fluxes. By way of example,
989 using the data in Fig. 7 on the right, a linear fit to the ground temperature at all
990 measured depths predicts $dT/dx \approx 45 \text{ }^\circ\text{C m}^{-1}$. In contrast, a two-point gradient
991 using the temperature at 0 and 10 cm depths, so only in the conductive zone, as
992 indicated in Fig.6, gives $dT/dx \approx 450 \text{ }^\circ\text{C m}^{-1}$. The actual conductive heat flux
993 (cf. eq. (1)) would thus be significantly higher than our estimation with a linear
994 fit over the entire depth, perhaps by as much as an order of magnitude.

995
996
997
998
999
1000
1001
1002
1003
1004
1005
1006
1007
1008
1009
1010
1011
1012

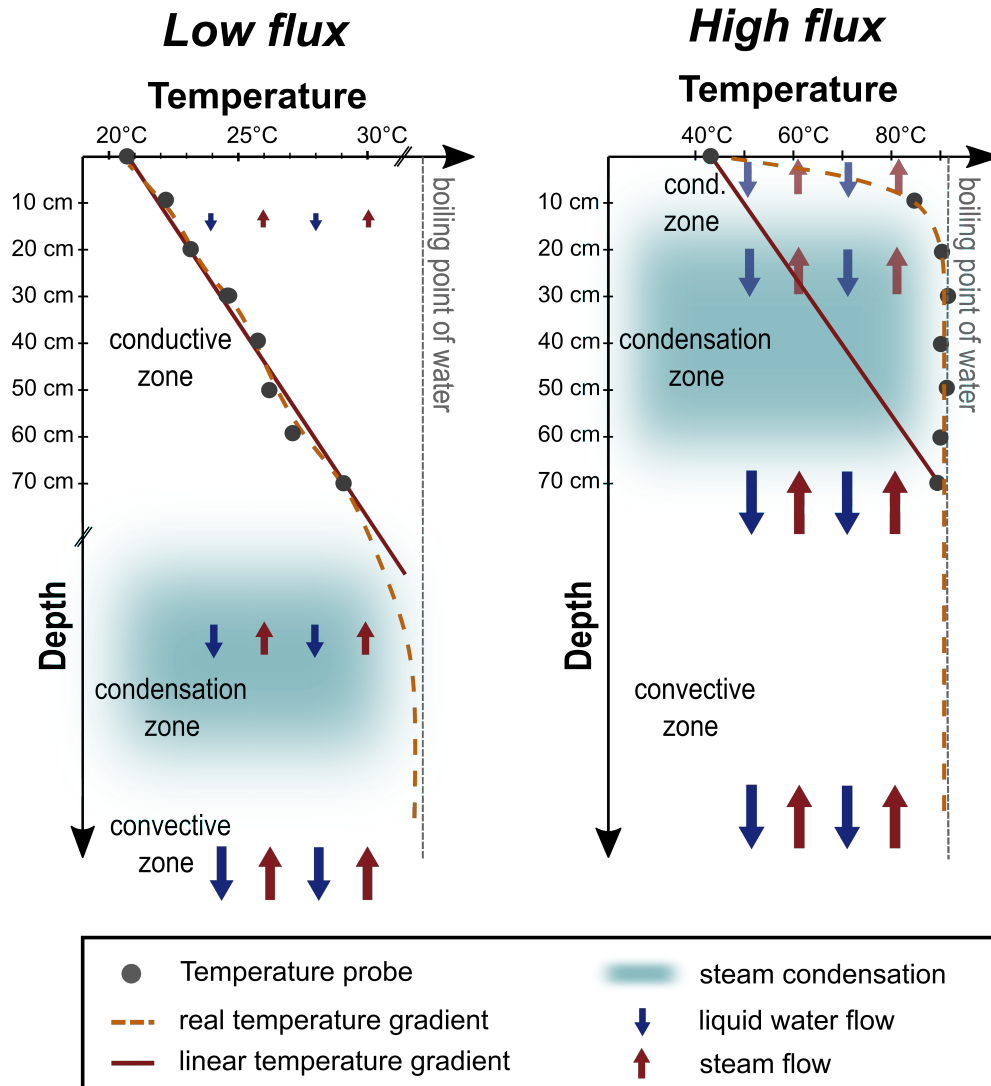


Fig. 7 Illustration of temperature profiles determined from the thermal probe measurements in low- and high-flux diffuse degassing areas. When the condensation zone is relatively deep, as in the left profile, heat is transported to the surface primarily by conduction (cf. eq. (3)), and the estimated linear temperature gradient closely approximates the data. In high flux areas where the condensation zone is very shallow (right temperature profile), a linear gradient poorly approximates the data. Hence, our modelled linear temperature gradients lead to systematic underestimation of the derived surface heat flux using eq. (3) in high flux areas. The temperature profiles shown were measured (left) above Gouffre '56 (Easting: 643 084 m, Northing: 1 774 201 m; WGS84, UTM zone 20N) and (right) close to the NAPN fumarole (Easting: 643 013 m, Northing: 1 774 252 m) within the ZFNN. Figure adapted from Gaudin et al (2017)

1013
1014
1015
1016
1017
1018
1019
1020
1021
1022
1023
1024
1025
1026
1027
1028
1029
1030
1031
1032
1033
1034
1035
1036
1037
1038
1039
1040
1041
1042
1043
1044
1045
1046
1047
1048
1049
1050
1051
1052
1053
1054
1055
1056
1057
1058

1059 The ground heat flux is due to fluids rising from depth. As discussed above,
 1060 H₂O typically condenses beneath the surface and so cannot be readily mea-
 1061 sured whereas CO₂ is non-condensable at near-atmospheric P-T conditions. We
 1062 estimate the steam flux, $\phi_{\text{H}_2\text{O}}$, from the CO₂ flux by assuming that the hydrother-
 1063 mal H₂O/CO₂ mass ratio in diffuse degassing zones is the same as in fumarole
 1064 vapours, since these result from the boiling of the deep hydrothermal aquifer
 1065 (Moretti et al, 2020a). Given the small heat capacity of CO₂ compared to water
 1066 and an average H₂O/CO₂ = 17.8 wt % (OVSG-IPGP, 2018–2023), heat transport
 1067 by CO₂ is negligible compared to that transported by H₂O. Thus the convective
 1068 heat flux is given by (Hochstein and Bromley, 2005; Fridriksson et al, 2006):

$$1069 \quad Q_{\text{conv}} = \int_A \frac{\text{H}_2\text{O}}{\text{CO}_2} \phi_{\text{CO}_2} (h_{v,95} - h_{l,19}) dA. \quad (4)$$

1070 Here, $h_{v,95} = 2668 \text{ kJ kg}^{-1}$ is the specific enthalpy of steam at 95 °C (condensa-
 1071 tion temperature at summit level) and $h_{l,19} = 83 \text{ kJ kg}^{-1}$ the specific enthalpy
 1072 of liquid water at ambient air temperature (19.1 °C) (Koretsky, 2012). Using Eq.
 1073 (4) with the data presented in Fig. 6, we estimate $Q_{\text{conv}} = 2.25 \pm 0.46 \text{ MW}$.

1074 Thus by Eq. (2), we estimate that the total ground heat flux (i.e. $Q_{\text{cond}} +$
 1075 Q_{conv}) is $2.93 \pm 0.78 \text{ MW}$. We note that despite being only roughly half the value
 1076 estimated by Jessop et al (2021) ($5.7 \pm 0.9 \text{ MW}$) from aerial thermal imagery as
 1077 the sum of radiant and advective fluxes from the surface, our estimation is of
 1078 the same order of magnitude and provides a lower bound for the “true” value.
 1079 The study of Jessop et al (2021) covered a slightly larger area on the southern
 1080 flank (about 100m further south of CS) and in the densely vegetated zone to
 1081 the east of the area investigated in this study (Fig. 4a). As far as the heated
 1082 zones are concerned, the two studies cover approximately the same area. However,
 1083 as described above, our temperature survey only partly covers the temperature
 1084 anomaly in the ZFNN due to dense vegetation east of the surveyed zone. The
 1085 aerial imagery of Jessop et al (2021) reached further to the east and thus may
 1086 have captured additional heated spots despite the dense vegetation cover.

1087 Our analyses can be put into a global context by considering how the heat
 1088 and CO₂ budgets at La Soufrière compare to those for other volcanic complexes.
 1089 To this end, we use the data set compiled by Harvey et al (2015) based on CO₂
 1090 degassing and plot them along with our data in Fig. 8. We find that La Soufrière’s
 1091 total heat output is larger only than that of the Comalito complex at Masaya but
 1092 over a small area compared to the 22 other sites. However, large complexes such
 1093 as calderas naturally have far larger total budgets hence the flux density is a fairer
 1094 comparison between structures of different sizes (Harvey et al, 2015; Jessop et al,
 1095 2021). La Soufrière has mean heat and CO₂ flux densities of 132 MW km^{-2} and
 1096 $189 \text{ t km}^{-2} \text{ d}^{-1}$, respectively. Based on heat flux density, these values are higher
 1097 than for some large caldera-type complexes such as Solfatara, Campi Fleigri and
 1098 Nisyros but below those of other dome-like structures such as Vulcano and White
 1099 Island (Whakaari). The CO₂ flux density at La Soufrière is similar to that at
 1100 Ischia and far higher again than at Nisyros.

1101 As noted by Jessop et al (2021), the geological and volcano-tectonic set-
 1102 ting will play a large role in determining these flux densities, along with the
 1103 catchment area for reservoir recharge (Harvey et al, 2015). La Soufrière de Guade-
 1104 loupe is indeed a volcanic dome associated with strong gas emissions that are
 related to the enhanced boiling activity of the hydrothermal reservoir and an

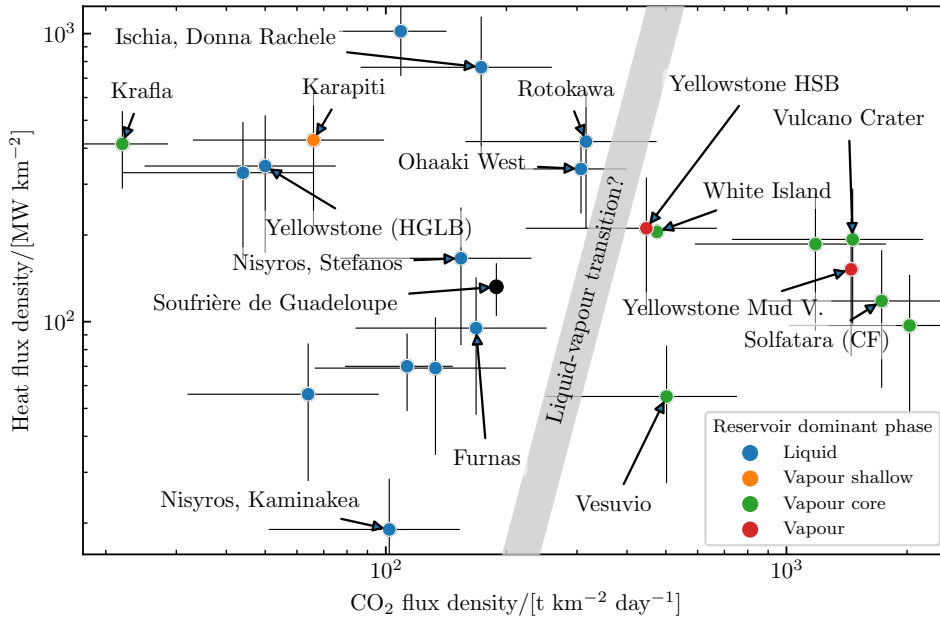


Fig. 8 Scatter plot of heat and CO₂ flux densities for a sample of hydrothermal volcanic systems. Here, the data (black dot: La Soufrière, this study; other data including error bars from Harvey et al, 2015) are classed in terms of the dominant phase in the reservoir (liquid/vapour). The grey bar indicates a suggested transition for the dominance of liquid to vapour. The slight top left to lower right trend for high heat flux/low CO₂ flux to low heat flux/high CO₂ flux is consistent with an increasing CO₂/H₂O ratio (see Fig. 1 in Harvey et al, 2015).

important proportion of hot magmatic gas vapour (Allard et al, 2014; Moretti et al, 2020a,b; Moune et al, 2022). Despite the low temperature of its fumarolic emissions which are close to the boiling temperature at the local height from La Soufrière's summit, Aiuppa et al (2017) include this volcano among high-temperature ($T \geq 450^\circ\text{C}$) arc volcanoes because of its high rate of emission and magmatic signature ($C/S \approx 2.3$). Regarding the compilations provided by Harvey et al (2015) and Aiuppa et al (2017), we note that Fig. 8 includes White Island and Vulcano, also dome volcanoes, which both fall in the vapour-dominated region and display high-temperature ($T > 700^\circ\text{C}$) fumaroles. La Soufrière hydrothermal system is marked by P-T conditions which often approach the water critical point (Moretti et al, 2020a), and by the rapid transit of hot, deep magmatic gases (Allard et al, 2014; Moune et al, 2022; Metcalfe et al, 2023). Although sufficient to hydrothermally re-equilibrate acid species (e.g. CO₂, H₂S, SO₂, HF and HCl) these typically do not deplete the S-bearing species as is observed in mature hydrothermal systems dominated by the liquid. As a result, the high flux, low-temperature steam discharges do not indicate a large hydrothermal system close to the maturity condition typically marked by mofete-like emissions at about 100 °C, nor a vast and deep liquid reservoir in which acid gases of magmatic origin are efficiently scrubbed, obliterating the magmatic source signature. Instead,

1151 as also shown by isotopic measurements (e.g. Villemant et al 2014), the high
 1152 flux, low-temperature steam released at La Soufrière reflects the considerable
 1153 contribution of meteoric water due to the heavy rainfall of a tropical environ-
 1154 ment (OVSG-IPGP, 1992–2023). We thus conjecture that rain saturation at the
 1155 La Soufrière volcanic-hydrothermal system is responsible for its closeness to the
 1156 inferred liquid-vapour transition. Furthermore, without such a contribution, La
 1157 Soufrière would likely fall into the vapour-dominated region, at higher values of
 1158 CO₂ flux density, due to the relatively lower absorption in circulating ground
 1159 waters and water droplets in the soil.

1160 **5.3 Spatial variations in the dominant mode of heat** 1161 **transport and depth of condensation imply spatially** 1162 **heterogeneous permeability** 1163

1164 From the temperature profiles calculated above, we can estimate the depth at
 1165 which the vapour begins to condense, x_c , from the root of

$$1166 T(x) - T_c = 0, \tag{5}$$

1167 where $T(x)$ given by Eq. (1) and $T_c \approx 95^\circ\text{C}$ which we solve using Newton’s
 1168 method. We also note that many sites have approximately zero temperature gra-
 1169 dient, a , inferring that $T \ll T_c$. We interpret this as meaning that condensation
 1170 will not occur in the near subsurface (i.e. in the first few metres). Where the
 1171 gradients were approximately zero, we dropped these from our data set and inter-
 1172 polated the remaining values (59 out of 110 values). From the result, shown in
 1173 Fig. 9, we note that x_c is on the order of a few tens of cm in the ZFNN and above
 1174 the Fractures Lacroix, and increases to many metres elsewhere.

1175 In areas where condensation occurs at depths greater than our measurements,
 1176 one would expect heat transport by pure conduction, resulting in a linear tem-
 1177 perature profile (constant gradient). Thus, one way to discriminate between the
 1178 relative effects of conductive and convective heat transfer is to determine the
 1179 linearity of the temperature profile. We do this by calculating Pearson’s R^2 coef-
 1180 ficient of determination from the linear regression of temperature with depth (cf.
 1181 Ricci et al, 2015). The R^2 value measures how well a linear (i.e. conduction)
 1182 model captures the data. Thus, $R^2 = 1$ where heat transfer is purely conductive
 1183 whereas low values of R^2 indicate that convection is the dominant mode of heat
 1184 transport. Our results are shown in Fig. 9 along with the interpolated map of
 1185 condensation depths. From the combination of these data, we determine that the
 1186 condensation isotherm in the ZFNN is very close to the surface. To the east of
 1187 NAPN (specifically in the quadrant east of 643 010 m E and north of 1 774 225 m
 1188 N in the local UTM), the profiles are typically linear: over 50% of this sub-
 1189 population of measurement sites have $R^2 > 0.925$. However, the other half of the
 1190 population has $0.6 < R^2 < 0.925$ (see Fig. 9) indicating that convection is an
 1191 important mode of heat transport in this region. This also becomes clear when
 1192 comparing Fig. 4a) and Fig. 4b): while the temperature gradient in the above-
 1193 mentioned quadrant is relatively small in many parts ($< 45^\circ\text{C m}^{-1}$, especially at
 1194 the easternmost boundary of the quadrant), the measured ground temperatures
 1195 at 20 cm depth range between 60 and 94.5 °C. Temperature gradients there are
 1196 small because convection and the associated near-surface condensation (cf. Fig.

7) result in high ground temperatures up to the surface (reflected in the relatively low R^2 values mentioned). In other areas, either the profiles are close to linear or the condensation depth is very deep (cf. the western portion of our measurement sites) which indicates that conduction is dominant.

We are aware that basing the R^2 on only 3 data points (versus 4 data points in Ricci et al 2015) limits the robustness of our analyses. However, since we are not interested in the exact R^2 value, but only in the deviation from linearity, we still consider this method valid to get an idea of the spatial variations of the conductive versus convective heat transfer mode. This is supported by the fact that the distribution of calculated R^2 values is consistent with what we see from our SP, CO₂ and temperature data.

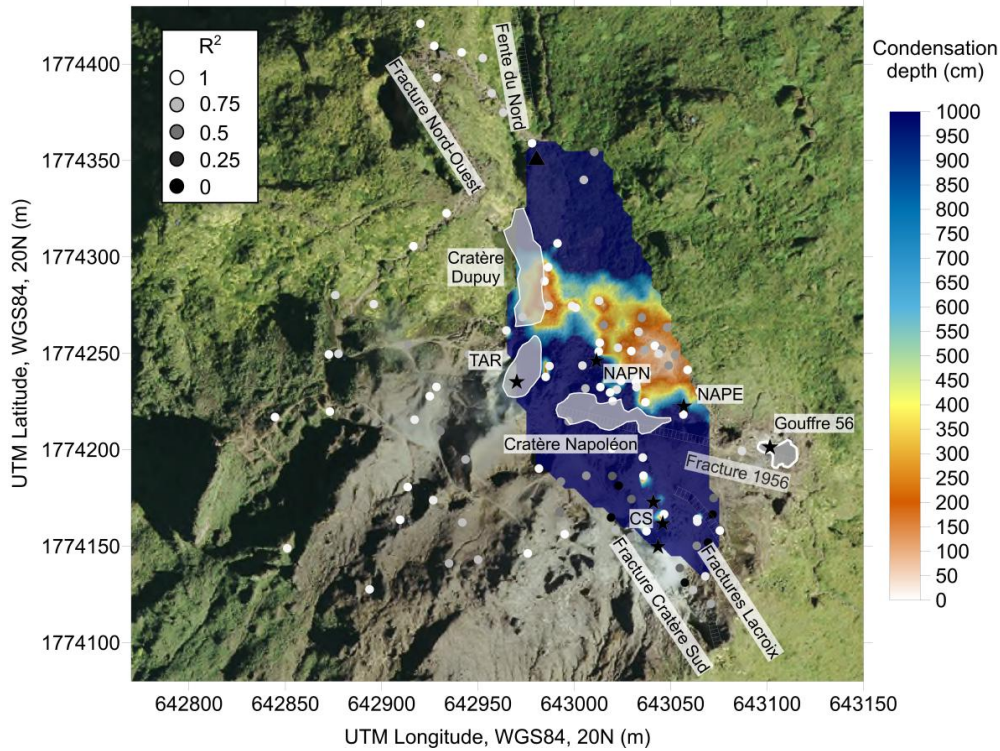


Fig. 9 Interpolated (sGs) map of condensation depths estimated from Eq. (5) overlain by the local value of Pearson's R^2 coefficient of determination. The R^2 value is used as an indicator of how well a linear temperature model describes the data, allowing us to discriminate between the relative effects of conductive and convective heat transfer (cf. Ricci et al, 2015). $R^2 = 1$ means that heat transfer is purely conductive, whereas low values of R^2 indicate an essential contribution of convection. The map shows the mean values of the 250 realisations in individual model cells (5×5 m) superimposed on an orthophoto of La Soufrière. Points at which temperature gradients were approximately zero were excluded from the estimation of condensation depth. No value indicates that the condensation depth is beyond 10 m. Black stars indicate the main summit fumaroles: Cratère Sud (CS), Gouffre '56, Napoléon Nord (NAPN), Napoléon Est (NAPE) and Tarissan (TAR). The area east of Cratère Dupuy/TAR and north of Cratère Napoléon is denoted ZFNN (cf. Fig. 1b and c)

1243 The combination of these results supports the hypothesis (cf. 5.2) that high
1244 ground temperatures, diffuse CO₂ fluxes and SP values in the ZFNN might be due
1245 to increased ground permeability. Increased subsurface permeability promotes
1246 vapour condensation near the surface and, owing to the high heat capacity and
1247 latent heat of water vapour, increased heat transport and more extensive ground
1248 heating (compare Fig. 4). That few temperature anomalies are seen near the
1249 major fumaroles (CS, G56 and Tarrisan) is in keeping with the hypothesis of
1250 impermeable sealing by deposits of sulphur-bearing minerals (Moune et al, 2022).
1251 Heap et al (2021b) sampled rocks from various locations on La Soufrière to
1252 study the degree of alteration and porosity of rocks forming the dome. They did
1253 not sample any rocks directly in the ZFNN; however, from our observations, the
1254 rock and soil in the ZFNN essentially correspond to what is also prevalent at the
1255 summit sampling locations of Heap et al (2021b). Rocks sampled close to summit
1256 fumaroles (Cratère Sud, Fractures Lacroix) showed secondary mineral assem-
1257 blages typical for intense acid fluid-rock interaction promoted by the efficient
1258 circulation of hydrothermal fluids. They further found that sampled andesites
1259 from La Soufrière are more porous than andesites from other stratovolcanoes.
1260 This result is supported by muon (Lesparre et al, 2012) and electrical tomogra-
1261 phy (Rosas-Carbajal et al, 2016), which have indicated that the material forming
1262 the edifice has a low density and most probably comprises high-porosity rocks.
1263 Seismic, geochemical and deformation data do not indicate any major changes
1264 in the magmatic-hydrothermal system (e.g. a rise in thermal input) but sup-
1265 port the hypothesis that observed high ground temperatures, diffuse CO₂ fluxes
1266 and SP values in the ZFNN are due to alteration and/or increased ground
1267 permeability.
1268 Seismicity is mainly superficial (typically <1 km below the summit) and can be
1269 interpreted as originating from the shallow hydrothermal system (Moretti et al,
1270 2020a, OVSG-IPGP 2020–2023). GNSS and extensometry stations located on
1271 the summit and flanks of La Soufrière show a mainly radial deformation centred
1272 on Cratère Tarissan and an opening of Cratère Napoléon (about 5 mm yr⁻¹
1273 until 2023), related to the sliding of the SW flank of the dome (Moretti et al,
1274 2020a, OVSG-IPGP 2018–2023). Deformation rates are essentially stationary and
1275 indicate no major change (inflation) in the deep system over the last ten years.
1276 The geochemical data also do not indicate a clear development in the magmatic
1277 system, although repeated injections of magmatic gases into the deep hydrother-
1278 mal system (2–3 km below the summit) have been observed since 2018 (Moretti
1279 et al, 2020a; Moune et al, 2022, OVSG-IPGP 2018–2023). Instead, fumarole
1280 degassing rate and temperature are mainly regulated by the amount of water in
1281 the hydrothermal aquifer (Inostroza et al, 2022; Moune et al, 2022). A relatively
1282 low water level in the hydrothermal aquifer could contribute to the observed
1283 larger spatial extent of ground heating and CO₂ degassing at the summit due to
1284 reduced damping of reservoir/fluid temperature and CO₂ absorption by ground-
1285 water, but would not explain the increased fluid circulation in the ZFNN that our
1286 SP data suggests. However, lower precipitation in recent years (average annual
1287 rainfall 2016–2021: 4.5 m, Vaerewyck (2022) vs. 1983–2010: 10 ± 2 m, Villemant
1288 et al (2014)) may also affect soil thermal properties and permeability (Heap
et al, 2020, 2023). While both the decreased water saturation of the system and
increased permeability could play a role in the observed changes, it remains to
be clarified which of the two factors is primary.

Future studies combining SP mapping with electrical resistivity tomography and possibly with induced polarisation tomography, as recently described in two reviews by Revil and Gresse (2021) and Revil et al (2023), could help to elucidate the structure of soil permeability further. The joint inversion of these data could provide valuable information about the depth and pattern of subsurface fluid flow as well as the current alteration state of the dome.

6 Conclusions

This paper presents the first combined mapping of SP, subsurface ground temperature and soil CO₂ flux on the summit of La Soufrière de Guadeloupe. These complementary methods allowed us to identify areas of fluid recharge into the hydrothermal system as well as the zones and extent of major ascending hydrothermal flows. A comparison of our data to previous work indicated spatial changes in shallow underground hydrothermal fluid circulation, which we explain with changing ground permeability distribution.

Based on our CO₂ flux measurements, we provide a first estimate of soil CO₂ degassing over the summit area, which amounts to $4.20 \pm 0.86 \text{ t d}^{-1}$, about half the CO₂ emissions from summit fumaroles. These data further suggest a convective ground heat flux of $2.25 \pm 0.46 \text{ MW}$ on the summit. Temperature gradients with depth derived from our soil temperature measurements allow us to get a lower bound estimate to conductive ground heat flux of $0.69 \pm 0.30 \text{ MW}$ comprising minimum and maximum rock thermal conductivity values. We thus obtain a total summit ground heat flux (fumaroles not taken into account) of $2.93 \pm 0.78 \text{ MW}$. We further determined the linearity of the temperature gradients with depth through Pearson's R^2 coefficient of determination, which along with the estimated condensation depths indicates that convection is an important mode of heat transport in the ZFNN (specifically in the quadrant east of 643 010 m E and north of 1 774 225 m N in the local UTM).

We find a heated (i.e. above ambient ground temperature) area of $22\,250 \pm 6\,900 \text{ m}^2$ on the summit, suggesting that ground heating has expanded since 2019 (Jessop et al, 2021). Both our 2022 temperature and SP surveys seem to cut off the ZFNN anomaly at the eastern edge of the survey area where deep vegetation starts. It is thus likely that the heated area in 2022 extended further to the E and NE and we conclude that the value has to be considered a lower bound estimate and that future efforts should be directed towards delimiting the eastern edge of subsurface fluid circulation. In line with the heated area estimate, we find a ground CO₂ degassing area of $26\,220 \pm 12\,550 \text{ m}^2$.

Maximum values of all measured parameters (CO₂ flux, ground temperature and SP) are located in the ZFNN indicating strong hydrothermal fluid circulation in that zone that we interpret as being a result of high sub-surface permeability. Comparison with previous studies shows that while the main rain infiltration zones seem to not have changed over time, we see a spatial development of the ascending flows. Repeated mapping will allow us to track the dynamic evolution of hydrothermal unrest and provide crucial information on the sealing extent of the dome.

The locations of flux maxima are delimited by prominent summit fractures: Fente du Nord, Dupuy and TAR to the west and Fracture 1956/Cratère Napoléon to the south. This implies a strong structural control of the observed dynamics

1335 underlined by the gradual opening of the W–E fractures between 2015 and 2021.
1336 We thus speculate that the increase in hydrothermal activity in the ZFNN could
1337 be related to the observed radial surface displacements on the summit (OVSG-
1338 IPGP, 2023) and the sliding of the SW flank (Rosas-Carbajal et al, 2016; Moretti
1339 et al, 2020a).
1340
1341
1342
1343
1344
1345
1346
1347
1348
1349
1350
1351
1352
1353
1354
1355
1356
1357
1358
1359
1360
1361
1362
1363
1364
1365
1366
1367
1368
1369
1370
1371
1372
1373
1374
1375
1376
1377
1378
1379
1380

1381
1382
1383
1384
1385
1386
1387
1388
1389
1390
1391
1392
1393
1394
1395
1396
1397
1398
1399
1400
1401
1402
1403
1404
1405
1406
1407
1408
1409
1410
1411
1412
1413
1414
1415
1416
1417
1418
1419
1420
1421
1422
1423
1424
1425
1426

7 Appendix

1427
 1428
 1429
 1430
 1431
 1432
 1433
 1434
 1435
 1436
 1437
 1438
 1439
 1440
 1441
 1442
 1443
 1444
 1445
 1446
 1447
 1448
 1449
 1450
 1451
 1452
 1453
 1454
 1455
 1456
 1457
 1458
 1459
 1460
 1461
 1462
 1463
 1464
 1465
 1466
 1467
 1468
 1469
 1470
 1471
 1472

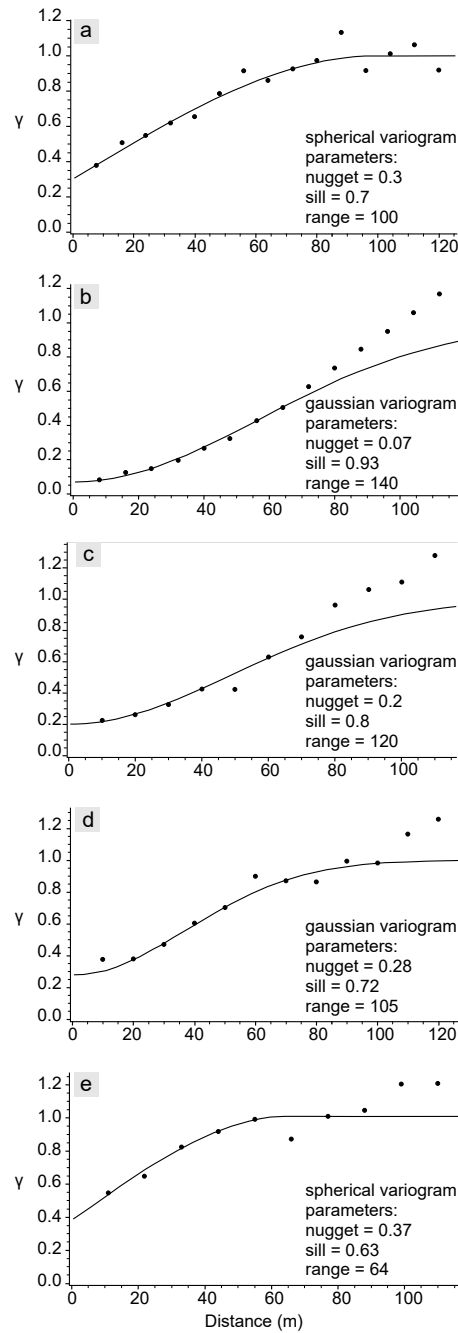


Fig. 10 Omnidirectional experimental variograms (γ) of normal score data: (a) soil CO₂ flux, (b) SP, (c) ground temperature at 20 cm depth, (d) ground temperature gradient, and (e) condensation depth. Lines represent the isotropic variogram models used in sGs interpolations. The outcome of the simulations is presented in Fig. 2, 4, 6, 9

References

- Aiuppa A, Fischer TP, Plank T, et al (2017) Along-arc, inter-arc and arc-to-arc variations in volcanic gas CO_2/S_T ratios reveal dual source of carbon in arc volcanism. *Earth-Science Reviews* 168:24–47. <https://doi.org/https://doi.org/10.1016/j.earscirev.2017.03.005>, URL <https://www.sciencedirect.com/science/article/pii/S0012825217300028>
- Aizawa K (2008) Classification of self-potential anomalies on volcanoes and possible interpretations for their subsurface structure. *Journal of Volcanology and Geothermal Research* 175:253–268. <https://doi.org/10.1016/j.jvolgeores.2008.03.011>
- Aizawa K, Ogawa Y, Ishido T (2009) Groundwater flow and hydrothermal systems within volcanic edifices: Delineation by electric self-potential and magnetotellurics. *Journal of Geophysical Research: Solid Earth* 114(1). <https://doi.org/10.1029/2008JB005910>, URL <https://agupubs.onlinelibrary.wiley.com/doi/abs/10.1029/2008JB005910>
- Allard P, Aiuppa A, Beauducel F, et al (2014) Steam and gas emission rate from La Soufriere volcano, Guadeloupe (Lesser Antilles): Implications for the magmatic supply during degassing unrest. *Chemical Geology* 384:76–93. <https://doi.org/10.1016/j.chemgeo.2014.06.019>
- Aubert M (1999) Practical evaluation of steady heat discharge from dormant active volcanoes: case study of Vulcarolo fissure (Mount Etna, Italy). *J Volcanol Geoth Res* 92(3–4):413–429. [https://doi.org/10.1016/S0377-0273\(99\)00088-8](https://doi.org/10.1016/S0377-0273(99)00088-8)
- Barberi F, Bertagnini A, Landi P, et al (1992) A review on phreatic eruptions and their precursors. *Journal of Volcanology and Geothermal Research* 52(4):231–246. [https://doi.org/https://doi.org/10.1016/0377-0273\(92\)90046-G](https://doi.org/https://doi.org/10.1016/0377-0273(92)90046-G), URL <https://www.sciencedirect.com/science/article/pii/037702739290046G>
- Barde-Cabusson S, Finizola A, Revil A, et al (2009) New geological insights and structural control on fluid circulation in La Fossa cone (Vulcano, Aeolian Islands, Italy). *Journal of Volcanology and Geothermal Research* 185(3):231–245. <https://doi.org/https://doi.org/10.1016/j.jvolgeores.2009.06.002>, URL <https://www.sciencedirect.com/science/article/pii/S037702730900242X>
- Barde-Cabusson S, Finizola A, Peltier A, et al (2012) Structural control of collapse events inferred by self-potential mapping on the Piton de la Fournaise volcano (La Réunion Island). *Journal of Volcanology and Geothermal Research* 209–210:9–18. <https://doi.org/https://doi.org/10.1016/j.jvolgeores.2011.09.014>, URL <https://www.sciencedirect.com/science/article/pii/S0377027311002575>
- Barde-Cabusson S, Finizola A, Grobde N, et al (2021) A practical approach for self-potential data acquisition, processing, and visualization. *Interpretation* 9:T123–T143. <https://doi.org/10.1190/int-2020-0012.1>, URL <https://hal.univ-reunion.fr/>

1519 [hal-03003692](#)
1520
1521 Boudon G, Semet MP, Vincent PM (1984) Flank failure–directed blast eruption at
1522 Soufrière, Guadeloupe, French West Indies: a 3,000-yr-old Mt. St. Helens ? *Geology*
1523 12(6):350–353. [https://doi.org/10.1130/0091-7613\(1984\)12<350:FFBEAS>2.0.CO;2](https://doi.org/10.1130/0091-7613(1984)12<350:FFBEAS>2.0.CO;2),
1524 URL [https://doi.org/10.1130/0091-7613\(1984\)12<350:FFBEAS>2.0.CO;2](https://doi.org/10.1130/0091-7613(1984)12<350:FFBEAS>2.0.CO;2)
1525
1526 Boudon G, Komorowski JC, Villemant B, et al (2008) A new scenario for the last mag-
1527 matic eruption of La Soufrière of Guadeloupe (Lesser Antilles) in 1530 AD: evidence
1528 from stratigraphy, radiocarbon dating and magmatic evolution of erupted products.
1529 *J Volcanol Geoth Res* 178(3):474–490. [https://doi.org/10.1016/j.jvolgeores.2008.03.](https://doi.org/10.1016/j.jvolgeores.2008.03.006)
1530 006
1531
1532 Brothelande E, Finizola A, Peltier A, et al (2014) Fluid circulation pattern inside
1533 La Soufrière volcano (Guadeloupe) inferred from combined electrical resistivity
1534 tomography, self-potential, soil temperature and diffuse degassing measurements. *J*
1535 *Volcanol Geoth Res* 288:105–122. <https://doi.org/10.1016/j.jvolgeores.2014.10.007>,
1536 URL <https://hal.univ-reunion.fr/hal-01391280>
1537
1538 Byrdina S, Vandemeulebrouck J, Cardellini C, et al (2014) Relations between
1539 electrical resistivity, carbon dioxide flux, and self-potential in the shallow
1540 hydrothermal system of Solfatara (Phlegrean Fields, Italy). *Journal of Volcanology*
1541 *and Geothermal Research* 283:172–182. [https://doi.org/https://doi.org/10.1016/](https://doi.org/https://doi.org/10.1016/j.jvolgeores.2014.07.010)
1542 [j.jvolgeores.2014.07.010](https://doi.org/https://doi.org/10.1016/j.jvolgeores.2014.07.010), URL [https://www.sciencedirect.com/science/article/pii/](https://www.sciencedirect.com/science/article/pii/S0377027314002212)
1543 [S0377027314002212](https://www.sciencedirect.com/science/article/pii/S0377027314002212)
1544
1545 Cardellini C, Chiodini G, Frondini F (2003) Application of stochastic simula-
1546 tion to CO₂ flux from soil: Mapping and quantification of gas release. *Journal*
1547 *of Geophysical Research: Solid Earth* 108(B9). [https://doi.org/https://doi.org/](https://doi.org/https://doi.org/10.1029/2002JB002165)
1548 [10.1029/2002JB002165](https://doi.org/https://doi.org/10.1029/2002JB002165), URL [https://agupubs.onlinelibrary.wiley.com/doi/abs/10.](https://agupubs.onlinelibrary.wiley.com/doi/abs/10.1029/2002JB002165)
1549 [1029/2002JB002165](https://agupubs.onlinelibrary.wiley.com/doi/abs/10.1029/2002JB002165)
1550
1551 Cardellini C, Chiodini G, Frondini F, et al (2017) Monitoring diffuse volcanic degassing
1552 during volcanic unrests: The case of Campi Flegrei (Italy). *Scientific Reports* 7.
1553 <https://doi.org/10.1038/s41598-017-06941-2>
1554
1555 Chiodini G, Frondini F, Raco B (1996) Diffuse emission of CO₂ from the Fossa crater,
1556 Vulcano Island (Italy). *Bulletin of Volcanology* 58:41–50. [https://doi.org/10.1007/](https://doi.org/10.1007/s004450050124)
1557 [s004450050124](https://doi.org/10.1007/s004450050124), URL <https://doi.org/10.1007/s004450050124>
1558
1559 Chiodini G, Cioni R, Guidi M, et al (1998) Soil CO₂ flux measurements in vol-
1560 canic and geothermal areas. *Applied Geochemistry* 13(5):543–552. [https://doi.org/](https://doi.org/https://doi.org/10.1016/S0883-2927(97)00076-0)
1561 [https://doi.org/10.1016/S0883-2927\(97\)00076-0](https://doi.org/https://doi.org/10.1016/S0883-2927(97)00076-0), URL [https://www.sciencedirect.](https://www.sciencedirect.com/science/article/pii/S0883292797000760)
1562 [com/science/article/pii/S0883292797000760](https://www.sciencedirect.com/science/article/pii/S0883292797000760)
1563
1564 Chiodini G, Frondini F, Cardellini C, et al (2001) CO₂ degassing and energy release
at Solfatara volcano, Campi Flegrei, Italy. *Journal of Geophysical Research: Solid*

- Earth 106(B8):16213–16221. <https://doi.org/10.1029/2001JB000246>, URL <https://agupubs.onlinelibrary.wiley.com/doi/abs/10.1029/2001JB000246> 1565
1566
1567
- Chiodini G, Granieri D, Avino R, et al (2005) Carbon dioxide diffuse degassing and estimation of heat release from volcanic and hydrothermal systems. *J Geophys Res* 110(B8):1–17. <https://doi.org/10.1029/2004JB003542> 1568
1569
1570
1571
- Corwin RF, Hoover DB (1979) The self-potential method in geothermal exploration. *GEOPHYSICS* 44(2):226–245. <https://doi.org/10.1190/1.1440964>, URL <https://doi.org/10.1190/1.1440964> 1572
1573
1574
1575
- Dempsey DE, Cronin SJ, Mei S, et al (2020) Automatic precursor recognition and real-time forecasting of sudden explosive volcanic eruptions at Whakaari, New Zealand. *Nature Communications* 11. <https://doi.org/10.1038/s41467-020-17375-2> 1576
1577
1578
1579
- Elío J, Ortega M, Nisi B, et al (2016) A multi-statistical approach for estimating the total output of CO₂ from diffuse soil degassing by the accumulation chamber method. *Int J Greenh Gas Control* 47:351–363. <https://doi.org/10.1016/j.ijggc.2016.02.012> 1580
1581
1582
1583
- Farquharson J, Wild B, Kushnir A, et al (2019) Acid-induced dissolution of andesite: Evolution of permeability and strength. *Journal of Geophysical Research : Solid Earth* 124:257–273. <https://doi.org/10.1029/2018JB016130>, URL <https://hal.science/hal-02376607> 1584
1585
1586
1587
1588
- Feuillard M, Allegre C, Brandeis G, et al (1983) The 1975–1977 crisis of La Soufriere de Guadeloupe (F.W.I): A still-born magmatic eruption. *Journal of Volcanology and Geothermal Research* 16(3):317–334. [https://doi.org/https://doi.org/10.1016/0377-0273\(83\)90036-7](https://doi.org/https://doi.org/10.1016/0377-0273(83)90036-7), URL <https://www.sciencedirect.com/science/article/pii/0377027383900367> 1589
1590
1591
1592
1593
1594
- Feuillet N, Manighetti I, Tapponnier P, et al (2002) Arc parallel extension and localization of volcanic complexes in Guadeloupe, Lesser Antilles. *Journal of Geophysical Research: Solid Earth* 107(B12):ETG 3–1–ETG 3–29. <https://doi.org/https://doi.org/10.1029/2001JB000308>, URL <https://agupubs.onlinelibrary.wiley.com/doi/abs/10.1029/2001JB000308> 1595
1596
1597
1598
1599
1600
- Finizola A, Sortino F, Lénat JF, et al (2002) Fluid circulation at Stromboli volcano (Aeolian Islands, Italy) from self-potential and CO₂ surveys. *J Volcanol Geoth Res* 116(1):1–18. [https://doi.org/10.1016/S0377-0273\(01\)00327-4](https://doi.org/10.1016/S0377-0273(01)00327-4), URL <https://hal.archives-ouvertes.fr/hal-01452542> 1601
1602
1603
1604
1605
- Finizola A, Lénat JF, Macedo O, et al (2004) Fluid circulation and structural discontinuities inside Misti volcano (Peru) inferred from self-potential measurements. *J Volcanol Geoth Res* 135. <https://doi.org/10.1016/j.jvolgeores.2004.03.009>, URL <https://hal.archives-ouvertes.fr/hal-01452539> 1606
1607
1608
1609
1610

- 1611 Finizola A, Ricci T, Deiana R, et al (2010) Adventive hydrothermal circulation on
1612 Stromboli volcano (Aeolian Islands, Italy) revealed by geophysical and geochemi-
1613 cal approaches: Implications for general fluid flow models on volcanoes. *Journal of*
1614 *Volcanology and Geothermal Research* 196(1-2):111–119. [https://doi.org/10.1016/](https://doi.org/10.1016/J.JVOLGEORES.2010.07.022)
1615 [J.JVOLGEORES.2010.07.022](https://doi.org/10.1016/J.JVOLGEORES.2010.07.022), URL <https://insu.hal.science/insu-00564998>
1616
- 1617 Fischer TP, Chiodini G (2015) Volcanic, Magmatic and Hydrothermal Gases. In: Sig-
1618 urdsson H (ed) *The Encyclopedia of Volcanoes (Second Edition)*, second edition edn.
1619 Academic Press, Amsterdam, p 779–797, [https://doi.org/https://doi.org/10.1016/](https://doi.org/https://doi.org/10.1016/B978-0-12-385938-9.00045-6)
1620 [B978-0-12-385938-9.00045-6](https://doi.org/https://doi.org/10.1016/B978-0-12-385938-9.00045-6), URL [https://www.sciencedirect.com/science/article/](https://www.sciencedirect.com/science/article/pii/B9780123859389000456)
1621 [pii/B9780123859389000456](https://www.sciencedirect.com/science/article/pii/B9780123859389000456)
1622
- 1623 Fridriksson T, Kristjánsson BR, Ármannsson H, et al (2006) CO₂ emissions and heat
1624 flow through soil, fumaroles, and steam heated mud pools at the Reykjanes geother-
1625 mal area, SW Iceland. *Applied Geochemistry* 21(9):1551–1569. [https://doi.org/](https://doi.org/https://doi.org/10.1016/j.apgeochem.2006.04.006)
1626 [https://doi.org/10.1016/j.apgeochem.2006.04.006](https://doi.org/https://doi.org/10.1016/j.apgeochem.2006.04.006), URL [https://www.sciencedirect.](https://www.sciencedirect.com/science/article/pii/S0883292706001235)
1627 [com/science/article/pii/S0883292706001235](https://www.sciencedirect.com/science/article/pii/S0883292706001235)
1628
- 1629 Gaudin D, Finizola A, Delcher E, et al (2015) Influence of rainfalls on heat and steam
1630 fluxes of fumarolic zones: six months records along the Ty Fault (Soufrière of Guade-
1631 loupe, Lesser Antilles). *J Volcanol Geoth Res* 302:273–285. [https://doi.org/10.1016/](https://doi.org/10.1016/j.jvolgeores.2015.06.015)
1632 [j.jvolgeores.2015.06.015](https://doi.org/10.1016/j.jvolgeores.2015.06.015), URL [https://www.sciencedirect.com/science/article/pii/](https://www.sciencedirect.com/science/article/pii/S0377027315001912)
1633 [S0377027315001912](https://www.sciencedirect.com/science/article/pii/S0377027315001912)
1634
- 1635 Gaudin D, Beauducel F, Coutant O, et al (2016) Mass and heat flux balance of
1636 La Soufrière volcano (Guadeloupe) from aerial infrared thermal imaging. *Journal*
1637 *of Volcanology and Geothermal Research* 320:107–116. [https://doi.org/10.1016/j.](https://doi.org/10.1016/j.jvolgeores.2016.04.007)
1638 [jvolgeores.2016.04.007](https://doi.org/10.1016/j.jvolgeores.2016.04.007)
1639
- 1640 Gaudin D, Ricci T, Finizola A, et al (2017) Heat flux-based strategies for the thermal
1641 monitoring of sub-fumarolic areas: Examples from Vulcano and La Soufrière de
1642 Guadeloupe. *Journal of Volcanology and Geothermal Research* 343:122–134. <https://doi.org/10.1016/j.jvolgeores.2017.06.021>
1643
- 1644 Grobde N, Barde-Cabusson S (2019) Self-Potential Studies in Volcanic Environ-
1645 ments: A Cheap and Efficient Method for Multiscale Fluid-Flow Investigations.
1646 *International Journal of Geophysics* 2019. <https://doi.org/10.1155/2019/2985824>
1647
- 1648 Harris A, Maciejewski A (2000) Thermal surveys of the vulcano fossa fumarole
1649 field 1994–1999: evidence for fumarole migration and sealing. *Journal of Vol-*
1650 *canology and Geothermal Research* 102(1):119–147. [https://doi.org/https://doi.](https://doi.org/https://doi.org/10.1016/S0377-0273(00)00184-0)
1651 [org/10.1016/S0377-0273\(00\)00184-0](https://doi.org/https://doi.org/10.1016/S0377-0273(00)00184-0), URL [https://www.sciencedirect.com/science/](https://www.sciencedirect.com/science/article/pii/S0377027300001840)
1652 [article/pii/S0377027300001840](https://www.sciencedirect.com/science/article/pii/S0377027300001840)
1653
- 1654 Harris AJL (2013) *Thermal remote sensing of active volcanoes: a user’s manual.*
1655 Cambridge University Press
1656

- Harris AJL, Lodato L, Dehn J, et al (2009) Thermal characterization of the Vulcano fumarole field. *Bull Volcanol* 71(4):441–458. <https://doi.org/10.1007/s00445-008-0236-8> 1657
1658
1659
1660
- Harvey MC, Rowland JV, Chiodini G, et al (2015) Heat flux from magmatic hydrothermal systems related to availability of fluid recharge. *J Volcanol Geoth Res* 302:225–236. <https://doi.org/10.1016/j.jvolgeores.2015.07.003> 1661
1662
1663
1664
- Hase H, Ishido T, Takakura S, et al (2003) Zeta potential measurement of volcanic rocks from Aso caldera. *Geophysical Research Letters* 30(23). <https://doi.org/https://doi.org/10.1029/2003GL018694>, URL <https://agupubs.onlinelibrary.wiley.com/doi/abs/10.1029/2003GL018694> 1665
1666
1667
1668
1669
- Heap MJ, Troll VR, Kushnir AR, et al (2019) Hydrothermal alteration of andesitic lava domes can lead to explosive volcanic behaviour. *Nature Communications* 10. <https://doi.org/10.1038/s41467-019-13102-8> 1670
1671
1672
1673
- Heap MJ, Kushnir AR, Vasseur J, et al (2020) The thermal properties of porous andesite. *Journal of Volcanology and Geothermal Research* 398:106901. <https://doi.org/https://doi.org/10.1016/j.jvolgeores.2020.106901>, URL <https://www.sciencedirect.com/science/article/pii/S0377027320300925> 1674
1675
1676
1677
1678
- Heap MJ, Baumann T, Gilg HA, et al (2021a) Hydrothermal alteration can result in pore pressurization and volcano instability. *Geology* 49:1348–1352. <https://doi.org/10.1130/G49063.1> 1679
1680
1681
1682
- Heap MJ, Baumann TS, Rosas-Carbajal M, et al (2021b) Alteration-Induced Volcano Instability at La Soufrière de Guadeloupe (Eastern Caribbean). *Journal of Geophysical Research: Solid Earth* 126. <https://doi.org/10.1029/2021JB022514> 1683
1684
1685
1686
- Heap MJ, Jessop DE, Wadsworth FB, et al (2022) The thermal properties of hydrothermally altered andesites from La Soufrière de Guadeloupe (Eastern Caribbean). *J Volcanol Geoth Res* 421:107444. <https://doi.org/https://doi.org/10.1016/j.jvolgeores.2021.107444>, URL <https://www.sciencedirect.com/science/article/pii/S0377027321002730> 1687
1688
1689
1690
1691
- Heap MJ, Wadsworth FB, Jessop DE (2023) The thermal conductivity of unlithified granular volcanic materials: The influence of hydrothermal alteration and degree of water saturation. *J Volcanol Geoth Res* 435:107775. <https://doi.org/10.1016/j.jvolgeores.2023.107775>, URL <https://hal.uca.fr/hal-04005461v1> 1692
1693
1694
1695
1696
- Hedenquist JW, Lowenstern JB (1994) The role of magmas in the formation of hydrothermal ore deposits. *Nature* 370(6490):519–527. <https://doi.org/10.1038/370519a0> 1697
1698
1699
1700
- Hincks TK, Komorowski J, Sparks S, et al (2014) Retrospective analysis of uncertain eruption precursors at La Soufrière volcano, Guadeloupe, 1975–77: volcanic 1701
1702

1703 hazard assessment using a Bayesian Belief Network approach. *Journal of Applied*
1704 *Volcanology* 3:1–26. <https://doi.org/10.1186/2191-5040-3-3>
1705
1706 Hirn A, Michel B (1979) Evidence of migration of main shocks during major seismo-
1707 volcanic crises of La Soufrière (Guadeloupe, Lesser Antilles) in 1976. *Journal of*
1708 *Volcanology and Geothermal Research* 6(3):295–304. [https://doi.org/https://doi.org/10.1016/0377-0273\(79\)90007-6](https://doi.org/https://doi.org/10.1016/0377-0273(79)90007-6), URL <https://www.sciencedirect.com/science/article/pii/0377027379900076>
1709
1710
1711 Hochstein MP, Bromley CJ (2005) Measurement of heat flux from steaming ground.
1712 *Geothermics* 34(2):131–158. <https://doi.org/10.1016/j.geothermics.2004.04.002>
1713
1714 Hochstein MP, Browne PRL (2000) Surface manifestations of geothermal systems
1715 with volcanic heat sources. In: Sigurdsson H, Houghton B, Rymer H, et al (eds)
1716 *Encyclopedia of volcanoes*, 1st edn. Academic Press, San Diego, p 835–855
1717
1718 Hutchison W, Mather TA, Pyle DM, et al (2015) Structural controls on fluid pathways
1719 in an active rift system: A case study of the Aluto volcanic complex. *Geosphere*
1720 11(3):542–562. <https://doi.org/https://doi.org/10.1130/GES01119.1>, URL <https://pubs.geoscienceworld.org/gsa/geosphere/article-pdf/11/3/542/3332882/542.pdf>
1721
1722
1723 Inostroza M, Moune S, Moretti R, et al (2022) Monitoring Hydrothermal Activity
1724 Using Major and Trace Elements in Low-Temperature Fumarolic Condensates: The
1725 Case of La Soufrière de Guadeloupe Volcano. *Geosciences* 12(7). <https://doi.org/10.3390/geosciences12070267>, URL <https://www.mdpi.com/2076-3263/12/7/267>
1726
1727
1728 Jessop DE, Moune S, Moretti R, et al (2021) A multi-decadal view of the heat and
1729 mass budget of a volcano in unrest: La Soufrière de Guadeloupe (French West
1730 Indies). *Bull Volcanol* 83(3):16. <https://doi.org/10.1007/s00445-021-01439-2>, URL
1731 <https://hal.uca.fr/hal-02974046v2>
1732
1733 Jouniaux L, Ishido T (2012) Electrokinetics in earth sciences: A tutorial. *International*
1734 *Journal of Geophysics* 2012. <https://doi.org/10.1155/2012/286107>
1735
1736 Jouniaux L, Maineult A, Naudet V, et al (2009) Review of self-potential methods
1737 in hydrogeophysics. *Comptes Rendus - Geoscience* 341:928–936. <https://doi.org/10.1016/j.crte.2009.08.008>
1738
1739
1740 Karstens J, Berndt C, Urlaub M, et al (2019) From gradual spreading to catastrophic
1741 collapse – Reconstruction of the 1888 Ritter Island volcanic sector collapse from
1742 high-resolution 3D seismic data. *Earth and Planetary Science Letters* 517:1–13.
1743 <https://doi.org/10.1016/j.epsl.2019.04.009>
1744
1745 Kilgour G, Manville V, Pasqua FD, et al (2010) The 25 September 2007 eruption
1746 of Mount Ruapehu, New Zealand: Directed ballistics, surtseyan jets, and ice-slurry
1747 lahars. *J Volcanol Geoth Res* 191:1–14. <https://doi.org/10.1016/j.jvolgeores.2009.10.015>
1748

Komorowski JC, Boudon G, Semet M, et al (2005) Guadeloupe. In: Volcanic hazard atlas of the Lesser Antilles. Seismic Research Unit, the University of the West Indies, Trinidad and Tobago, W.I., p 65–102	1749 1750 1751 1752
Koretsky MD (2012) Engineering and Chemical Thermodynamics, 2nd edn., John Wiley & Sons, chap Appendix B: Steam Tables, pp 647–649	1753 1754 1755
Lesparre N, Gibert D, Marteau J, et al (2012) Density muon radiography of La Soufrière of Guadeloupe volcano: comparison with geological, electrical resistivity and gravity data. <i>Geophysical Journal International</i> 190(2):1008–1019. https://doi.org/https://doi.org/10.1111/j.1365-246X.2012.05546.x , URL https://onlinelibrary.wiley.com/doi/abs/10.1111/j.1365-246X.2012.05546.x	1756 1757 1758 1759 1760
Lewicki JL, Connor C, St-Amand K, et al (2003) Self-potential, soil CO ₂ flux, and temperature on Masaya volcano, Nicaragua. <i>Geophysical Research Letters</i> 30. https://doi.org/10.1029/2003GL017731	1761 1762 1763 1764
Lewis A, Hilley GE, Lewicki JL (2015) Integrated thermal infrared imaging and structure-from-motion photogrammetry to map apparent temperature and radiant hydrothermal heat flux at Mammoth Mountain, CA, USA. <i>J Volcanol Geoth Res</i> 303:16–24. https://doi.org/10.1016/j.jvolgeores.2015.07.025	1765 1766 1767 1768 1769
Lénat JF (2007) Retrieving Self Potential anomalies in a complex volcanic environment : a SP/elevation gradient approach. <i>Near Surface Geophysics</i> 5:161–170. https://doi.org/10.3997/1873-0604.2006028	1770 1771 1772 1773
López DL, Williams SN (1993) Catastrophic volcanic collapse: Relation to hydrothermal processes. <i>Science</i> 260:1794–1796. https://doi.org/10.1126/science.260.5115.1794	1774 1775 1776 1777
Maeno F, Nakada S, Oikawa T, et al (2016) Reconstruction of a phreatic eruption on 27 September 2014 at Ontake volcano, central Japan, based on proximal pyroclastic density current and fallout deposits the Phreatic Eruption of Mt. Ontake Volcano in 2014 5. <i>Volcanology. Earth, Planets and Space</i> 68. https://doi.org/10.1186/s40623-016-0449-6	1778 1779 1780 1781 1782
Massenet F, Pham VN (1985) Mapping and surveillance of active fissure zones on a volcano by the self-potential method, Etna, Sicily. <i>Journal of Volcanology and Geothermal Research</i> 24(3):315–338. https://doi.org/https://doi.org/10.1016/0377-0273(85)90075-7 , URL https://www.sciencedirect.com/science/article/pii/0377027385900757	1783 1784 1785 1786 1787 1788
Matsushima N, Michiwaki M, Okazaki N, et al (1990) Self-Potential Studies in Volcanic Areas(2) : Usu, Hokkaido Komaga-take and Me-akan. <i>Journal of the Faculty of Science, Hokkaido University Series 7, Geophysics</i> 8:465–477. URL https://www.researchgate.net/publication/37548954	1789 1790 1791 1792 1793 1794

1795 Metcalfe A, Moune S, Komorowski JC, et al (2022) Bottom-up vs top-down drivers of
 1796 eruption style: Petro-geochemical constraints from the holocene explosive activity
 1797 at La Soufrière de Guadeloupe. *Journal of Volcanology and Geothermal Research*
 1798 424:107488. <https://doi.org/10.1016/j.jvolgeores.2022.107488>, URL
 1799 <https://www.sciencedirect.com/science/article/pii/S0377027322000191>
 1800
 1801 Metcalfe A, Moune S, Moretti R, et al (2023) Volatile emissions from past eruptions
 1802 at La Soufrière de Guadeloupe (Lesser Antilles): insights into degassing processes
 1803 and atmospheric impacts. *Frontiers in Earth Science* 11. [https://doi.org/10.3389/](https://doi.org/10.3389/feart.2023.1143325)
 1804 [feart.2023.1143325](https://doi.org/10.3389/feart.2023.1143325), URL [https://www.frontiersin.org/articles/10.3389/feart.2023.](https://www.frontiersin.org/articles/10.3389/feart.2023.1143325)
 1805 [1143325](https://www.frontiersin.org/articles/10.3389/feart.2023.1143325)
 1806
 1807 Moretti R, Komorowski JC, Ucciani G, et al (2020a) The 2018 unrest phase at La
 1808 Soufrière of Guadeloupe (French West Indies) andesitic volcano: Scrutiny of a failed
 1809 but prodromal phreatic eruption. *J Volcanol Geoth Res* 393. [https://doi.org/10.](https://doi.org/10.1016/j.jvolgeores.2020.106769)
 1810 [1016/j.jvolgeores.2020.106769](https://doi.org/10.1016/j.jvolgeores.2020.106769)
 1811
 1812 Moretti R, Moune S, Robert V, et al (2020b) Intercomparison of geochemical tech-
 1813 niques at La Soufrière de Guadeloupe (FWI) volcano: their advantages and their
 1814 limits over a long-standing unrest. *Ital J Geosci* [https://doi.org/10.3301/IJG.2020.](https://doi.org/10.3301/IJG.2020.13)
 1815 [13](https://doi.org/10.3301/IJG.2020.13), URL <https://hal.archives-ouvertes.fr/hal-03092221v1>
 1816
 1817 Moune S, Moretti R, Burtin A, et al (2022) Gas monitoring of volcanic-hydrothermal
 1818 plumes in a tropical environment: the example of La Soufrière de Guadeloupe unrest
 1819 volcano (Lesser Antilles). *Frontiers in Earth Science* 10. [https://doi.org/10.3389/](https://doi.org/10.3389/feart.2022.795760)
 1820 [feart.2022.795760](https://doi.org/10.3389/feart.2022.795760), URL <https://hal.uca.fr/hal-03609801v1>
 1821
 1822 Nourbehecht B (1963) Irreversible Thermodynamic Effects in Inhomogeneous Media
 1823 and Their Application in Certain Geoelectric Problems. PhD thesis, Massachusetts
 1824 Institute of Technology
 1825
 1826 OVSG-IPGP (1992–2023) Bilans mensuels et annuels de l'activité volcanique de la
 1827 Soufrière de Guadeloupe et de la sismicité régionale. In: Annual and monthly activity
 1828 reports. Observatoire Volcanologique et Sismologique de la Guadeloupe
 1829
 1829 Pham V, Boyer D, Boudon G, et al (1990) Anomalies de polarisation spontanée sur
 1830 La Soufrière de Guadeloupe. Relation avec la structure interne du volcan. *C R Acad*
 1831 *Sci* 2:815–821
 1832
 1833 Pichavant M, Poussineau S, Lesne P, et al (2018) Experimental Parametrization of
 1834 Magma Mixing: Application to the AD 1530 Eruption of La Soufrière, Guade-
 1835 loupe (Lesser Antilles). *Journal of Petrology* 59:257–282. [https://doi.org/10.1093/](https://doi.org/10.1093/petrology/egy030)
 1836 [petrology/egy030](https://doi.org/10.1093/petrology/egy030)
 1837
 1838 Pritchard ME, Mather TA, McNutt SR, et al (2019) Thoughts on the criteria to
 1839 determine the origin of volcanic unrest as magmatic or non-magmatic. *Philosophical Transactions of the Royal Society A: Mathematical, Physical and Engineering*
 1840

Sciences 377. https://doi.org/10.1098/rsta.2018.0008	1841
	1842
Reid M, Sisson T, Brien D (2001) Volcano collapse promoted by hydrothermal alteration and edifice shape, Mount Rainier, Washington. <i>Geology</i> 29. <a href="https://doi.org/10.1130/0091-7613(2001)029<0779:VCPBHA>2.0.CO;2">https://doi.org/10.1130/0091-7613(2001)029<0779:VCPBHA>2.0.CO;2	1843
	1844
	1845
	1846
Reid ME (2004) Massive collapse of volcano edifices triggered by hydrothermal pressurization. <i>Geology</i> 32:373–376. https://doi.org/10.1130/G20300.1	1847
	1848
	1849
Remy N, Boucher A, Wu J (2009) <i>Applied Geostatistics with SGeMS: A User’s Guide</i> . Cambridge University Press, https://doi.org/https://doi.org/10.1017/CBO9781139150019	1850
	1851
	1852
	1853
Revil A (2002) Comment on “Rapid fluid disruption: A source for self-potential anomalies on volcanoes” by M. J. S. Johnston, J. D. Byerlee, and D. Lockner. <i>Journal of Geophysical Research</i> 107. https://doi.org/10.1029/2001jb000788	1854
	1855
	1856
	1857
Revil A, Gresse M (2021) Induced polarization as a tool to assess alteration in geothermal systems: A review. <i>Minerals</i> 11(9). https://doi.org/10.3390/min11090962 , URL https://www.mdpi.com/2075-163X/11/9/962	1858
	1859
	1860
Revil A, Schwaeger H, Cathles LM, et al (1999) Streaming potential in porous media 2. Theory and application to geothermal systems. <i>Journal of Geophysical Research: Solid Earth</i> 104:20033–20048. https://doi.org/10.1029/1999jb900090	1861
	1862
	1863
	1864
Revil A, Finizola A, Gresse M (2023) Self-potential as a tool to assess groundwater flow in hydrothermal systems: A review. <i>Journal of Volcanology and Geothermal Research</i> 437:107788. https://doi.org/https://doi.org/10.1016/j.jvolgeores.2023.107788 , URL https://www.sciencedirect.com/science/article/pii/S0377027323000458	1865
	1866
	1867
	1868
	1869
	1870
Ricci T, Finizola A, Barde-Cabusson S, et al (2015) Hydrothermal fluid flow disruptions evidenced by subsurface changes in heat transfer modality: The La Fossa cone of Vulcano (Italy) case study. <i>Geology</i> 43:959–962. https://doi.org/10.1130/G37015.1	1871
	1872
	1873
	1874
	1875
Rosas-Carbajal M, Komorowski JC, Nicollin F, et al (2016) Volcano electrical tomography unveils edifice collapse hazard linked to hydrothermal system structure and dynamics. <i>Scientific Reports</i> 6. https://doi.org/10.1038/srep29899	1876
	1877
	1878
	1879
Rouwet D, Sandri L, Marzocchi W, et al (2014) Recognizing and tracking volcanic hazards related to non-magmatic unrest: A review. <i>Journal of Applied Volcanology</i> 3. https://doi.org/10.1186/s13617-014-0017-3	1880
	1881
	1882
	1883
Salaün A, Villemant B, Gérard M, et al (2011) Hydrothermal alteration in andesitic volcanoes: Trace element redistribution in active and ancient hydrothermal systems of Guadeloupe (Lesser Antilles). <i>Journal of Geochemical Exploration</i> 111:59–83.	1884
	1885
	1886

1887 <https://doi.org/10.1016/j.gexplo.2011.06.004>
1888
1889 Schöpa A, Pantaleo M, Walter T (2011) Scale-dependent location of hydrother-
1890 mal vents: Stress field models and infrared field observations on the Fossa Cone,
1891 Vulcano Island, Italy. *Journal of Volcanology and Geothermal Research* 203(3):133–
1892 145. <https://doi.org/https://doi.org/10.1016/j.jvolgeores.2011.03.008>, URL <https://www.sciencedirect.com/science/article/pii/S0377027311000813>
1893
1894 Sinclair AJ (1974) Selection of threshold values in geochemical data using proba-
1895 bility graphs. *Journal of Geochemical Exploration* 3:129–149. [https://doi.org/10.](https://doi.org/10.1016/0375-6742(74)90030-2)
1896 [1016/0375-6742\(74\)90030-2](https://doi.org/10.1016/0375-6742(74)90030-2), URL [https://www.sciencedirect.com/science/article/](https://www.sciencedirect.com/science/article/pii/0375674274900302)
1897 [pii/0375674274900302](https://www.sciencedirect.com/science/article/pii/0375674274900302)
1898
1899 Sparks RS, Barclay J, Calder ES, et al (2002) Generation of a debris avalanche and
1900 violent pyroclastic density current on 26 December (Boxing Day) 1997 at Soufrière
1901 Hills Volcano, Montserrat. *Geological Society Memoir* 21:409–434. [https://doi.org/](https://doi.org/10.1144/GSL.MEM.2002.021.01.18)
1902 [10.1144/GSL.MEM.2002.021.01.18](https://doi.org/10.1144/GSL.MEM.2002.021.01.18)
1903
1904 Stevenson DS (1993) Physical models of fumarolic flow. *J Volcanol Geoth Res* 57(3–
1905 4):139–156. [https://doi.org/10.1016/0377-0273\(93\)90009-G](https://doi.org/10.1016/0377-0273(93)90009-G)
1906
1907 Tamburello G, Moune S, Allard P, et al (2019) Spatio-temporal relationships between
1908 fumarolic activity, hydrothermal fluid circulation and geophysical signals at an arc
1909 volcano in degassing unrest: La Soufrière of Guadeloupe (French West Indies).
1910 *Geosci* 9(11). <https://doi.org/10.3390/geosciences9110480>
1911
1912 Vaerewyck C (2022) Évolution géochimique du lac acide Tarissan, Soufrière de
1913 Guadeloupe: couplage à la modélisation hydrogéologique pour l'interprétation des
1914 variations temporelles des concentrations en éléments halogènes. Master's thesis,
1915 Institut de Physique du Globe de Paris (IPGP), Université Paris Cité
1916
1917 Villemant B, Komorowski JC, Dessert C, et al (2014) Evidence for a new shallow
1918 magma intrusion at La Soufrière of Guadeloupe (Lesser Antilles). Insights from
1919 long-term geochemical monitoring of halogen-rich hydrothermal fluids. *J Volcanol*
1920 *Geoth Res* 285:247–277. <https://doi.org/10.1016/j.jvolgeores.2014.08.002>
1921
1922 van Wyk de Vries B, Francis P (1997) Catastrophic collapse at stratovolcanoes
1923 induced by gradual volcano spreading. *Nature* 387:387–390. [https://doi.org/10.](https://doi.org/10.1038/387387a0)
1924 [1038/387387a0](https://doi.org/10.1038/387387a0)
1925
1926 Watters R, Zimbelman D, Bowman S, et al (2000) Rock Mass Strength Assessment
1927 and Significance to Edifice Stability, Mount Rainier and Mount Hood, Cascade
1928 Range Volcanoes. *Pure and applied geophysics* 157:957–976. [https://doi.org/10.](https://doi.org/10.1007/s000240050012)
1929 [1007/s000240050012](https://doi.org/10.1007/s000240050012)
1930
1931 Zlotnicki J, Boudon G, Le Mouél JL (1992) The volcanic activity of La Soufrière of
1932 Guadeloupe (Lesser Antilles): structural and tectonic implications. *J Volcanol Geoth*

Res 49(1):91–104. https://doi.org/10.1016/0377-0273(92)90006-Y	1933
	1934
Zlotnicki J, Feuillard M, Hammouya G (1994) Water Circulations on La Soufrière	1935
Volcano Inferred by Self-Potential Surveys (Guadeloupe, Lesser Antilles). Renew of	1936
Volcanic Activity ? J Geomag Geoelectr 46:797–813	1937
	1938
	1939
	1940
	1941
	1942
	1943
	1944
	1945
	1946
	1947
	1948
	1949
	1950
	1951
	1952
	1953
	1954
	1955
	1956
	1957
	1958
	1959
	1960
	1961
	1962
	1963
	1964
	1965
	1966
	1967
	1968
	1969
	1970
	1971
	1972
	1973
	1974
	1975
	1976
	1977
	1978